Spring 2020

Geology and Geophysics of the Mogollon Mining District and the Bearwallow Mountain 7.5 Minute Quadrangle, Catron County, New Mexico

Charles Frost Hoffman
Missouri State University, Hoffman27@live.missouristate.edu

GEOLOGY AND GEOPHYSICS OF THE MOGOLLON MINING DISTRICT AND THE BEARWALLOW MOUNTAIN 7.5 MINUTE QUADRANGLE, CATRON COUNTY, NEW MEXICO

A Master's Thesis

Presented to

The Graduate College of

Missouri State University

In Partial Fulfillment

Of the Requirements for the Degree

Master of Science, Geography and Geology

By

Charles Frost Hoffman

May 2020

GEOLOGY AND GEOPHYSICS OF THE MOGOLLON MINING DISTRICT AND THE BEARWALLOW MOUNTAIN 7.5 MINUTE QUADRANGLE, CATRON COUNTY, NEW MEXICO

Geography, Geology & Planning

Missouri State University, May 2020

Master of Science

Charles F. Hoffman

ABSTRACT

The Mogollon Mining District and the Bearwallow Mountain 7.5-minute quadrangle are located in southwestern New Mexico, and are comprised of mid-Tertiary volcanic rocks that were the result of voluminous eruptions within the Mogollon-Datil Volcanic Field.
This thesis aims to better understand the geology and structure of the Bearwallow Mountain 7.5-minute quadrangle and the Mogollon Mining District, and to analyze the use of Very Low Frequency electromagnetic techniques to delineate buried structures in volcanic terranes.
I use Very Low Frequency electromagnetic methods and field mapping to evaluate the effectiveness of the method, and to better understand the geology and ore bodies in the mining district. The results indicate that the VLF-EM method is effective at identifying known and unknown structures via variations in electromagnetic responses. The profiles analyzed in this thesis indicate conductive zones along known faults, as well as conductive zones not associated with faults. These results conclude that the VLF-EM method is effective at identifying buried structures, however it is difficult to differentiate the source of the conductivity. Therefore, it could be used to identify possible exploration targets, but not mineralization.

KEYWORDS: Mogollon Mining District, Mogollon-Datil Volcanic Field, Bursum Caldera, New Mexico Volcanic-Epithermal Deposit, VLF-EM Exploration

GEOLOGY AND GEOPHYSICS OF THE MOGOLLON MINING DISTRICT AND THE BEARWALLOW MOUNTAIN 7.5 MINUTE QUADRANGLE, CATRON COUNTY, NEW MEXICO

By

Charles Frost Hoffman

A Master's Thesis
Submitted to the Graduate College
Of Missouri State University
In Partial Fulfillment of the Requirements
For the Degree of Master's of Science, Geography and Geology

May 2020

Approved:

Gary S. Michelfelder, Ph.D., Thesis Committee Chair

Kevin Mickus, Ph.D., Committee Member

Matthew McKay, Ph.D., Committee Member

Julie Masterson, Ph.D., Dean of the Graduate College

ACKNOWLEDGEMENTS

The author would like to thank the faculty and staff of the Department of Geography, Geology, and Planning at Missouri State University for their guidance with this project. The author would also like to thank Megan Peitz and Loren Bohannon for assistance in the field. Also, thank you to John Peitz for snacks in the field. Thank you to Gary Michelfelder for developing this project, and assisting with field work logistics. Thank you to Kevin Mickus for assistance with assistance with data processing and conversations on geophysics. Thank you to Matt McKay for comments on the final map. This project was funded in part by the Missouri State University Graduate College and the U.S. Geological Survey EDMAP grant program.

TABLE OF CONTENTS

LIST OF TABLES

Manuscript 1

LIST OF FIGURES

Manuscript 1

Manuscript 2

INTRODUCTION

The region in and around the Mogollon Mining District has long been the focus of prospectors and geologists alike, due to the allure of silver and gold. Prospectors as early as 1825 noted the presence of silver-ore in the bedload of the stream, but gold was not discovered in the Mogollon Mining District until 1875 (Anderson, 1939; Ferguson, 1927). Presently, One World Investments Inc. holds significant mineral claims in the mining district, and is in the early stages of exploration. The principal target of their exploration effort is the vicinity of the Consolidated Mine, along the Queen Vein at the intersection of the Graveyard vein (Hiner, 2016). This mine was active from 1937 until 1942, when the war board shut down the operation. Cordex Syndicate started a drill program in 1984 to explore intersections of WNW faults and the Queen fault. This program ended in 1988 due to an economic downturn. In 2010, Cordex sold the Mogollon interests to Columbus Silver Corporation, who explored three additional areas: north of the Consolidated Mine project, Independence – Ida May fault intersections, and Last Chance – Anna fault intersections with the Queen fault. Each of these programs resulted in veins, but mineralization was weak. Stand Up Investments Limited purchased the Mogollon holdings in 2015, however, they determined that the Consolidated Mine project was not mineral resource quality, and that more drilling was needed to bring the project up to resource status (Hiner, 2016). Allegiant Gold Ltd. acquired the property rights in July 2017, and entered an agreement with Barrian Mining Corporation to acquire 100% interest in the Mogollon project by 2021. The Consolidated Mine Site is of interest as it was the last productive site in the district.

The aim of this study is to explore the geology and fault systems east of the Mogollon Mining District to further our understanding of the geologic history and spatial extent of the ore body. Additionally, this study aims to use Very Low Frequency Electromagnetic geophysical

methods to identify new targets for exploration near the Consolidated Mine area. Understanding the regional fault systems would aid in exploration efforts in and around the district. The VLF-EM surveys around the Consolidated Mine project provide a cheap and relatively easy system of subsurface exploration. The system identifies buried vertical conductors, such as mineralized veins and fractures. Furthermore, the VLF-EM survey could delineate smaller faults that could help determine the ages of different tectonic stress regimes represented in the district.

The following chapters present two manuscripts on the geology and geophysics east of the Mogollon Mining District and VLF-EM and magnetic analyses of the Consolidated Mine site. In the first paper, *Geologic Map of the Bearwallow Mountain 7.5-Minute Quadrangle, Catron County, New Mexico*, I present a new 1:24,000-scale geologic map of the Bearwallow Mountain 7.5-minute quadrangle. The accompanying report discusses the regional geology, volcanic stratigraphy, structure, and geophysics of the quadrangle. In this report, I determine that the Bursum caldera rim is north of Bearwallow Mountain, though it is covered by younger material. Faults in the quadrangle are between 27 Ma and 25 Ma, and younger than the faults associated with the Mogollon Mining District mineralization; and that no obvious mineralization is present, though some late-stage rhyolitic dikes caused extensive alteration in the southeastern corner of the quadrangle.

The second article, *VLF-EM and Magnetic Analysis of the Consolidated Mine Site, Mogollon Mining District, New Mexico*, attempts to delineate buried faults and veins near the Consolidated Mine project. This article presents findings from processed and filtered VLF-EM data, and inverted VLF-EM models. In addition, we compare these results to gridded VLF-EM and magnetic data. These surveys suggest a vertical conductive body along the Independence fault, and continues through the Queen fault toward the Graveyard fault. A similar linear feature

is observed in the gridded magnetic data, suggesting a buried conductor. Furthermore, the Queen fault is conductive in some locations, but not continuously, which may decrease the mineral resource potential. We suggest further exploration along the Independence vein, as economic mineralization may be present at depth.

MANUSCRIPT 1: GEOLOGIC MAP OF THE BEARWALLOW MOUNTAIN 7.5-MINUTE QUADRANGLE, CATRON COUNTY, NEW MEXICO

Introduction

The G*eologic Map of the Bearwallow Mountain 7.5-Minute Quadrangle, Catron County, New Mexico*, accompanies this report. The purpose of this report is to provide geologic context and history of the region, and to discuss geologic relationships observed while mapping. Included is a detailed description of geologic units, structural analysis, compiled geochronology, and local geophysics.

The Bearwallow Mountain 7.5-minute quadrangle is encompassed by the Mogollon Mountains in south-central Catron County and entirely within the boundary of the Gila National Forest. The western edge is approximately 2.5 miles east of the ghost town of Mogollon, while the eastern edge bisects the terminus of the Gilita Creek and Forest Road 119. The highest peak within the quadrangle is Bearwallow Mountain (9,953'), but contains several other notable peaks including Spring Mountain (9,683'), Cooney Peak (8,591'), Corner Mountain (9,938'), and Lost Lake Mountain (8,219'). The lowest point in the quadrangle is where Mineral Creek exits the quadrangle flowing west (6,480'). Mineral Creek, Deep Creek, Devils Creek, and Copper Creek drain the quadrangle west of Bearwallow Mountain, while Gilita Creek, and Willow Creek drain the quadrangle east of Bearwallow Mountain. The entire quadrangle is owned by the United States Department of Agriculture and managed by the United States Forest Service, under the jurisdiction of Gila National Forest. Access is provided primarily by the Bursum Road (New Mexico Route 159) and the Bursum Fire Road in the south, and Forest Service roads 180 and

153 in the north. Access to the western quadrangle is limited to Copper Creek Road (Forest Service road 119).

Weber and Willard (1959) first mapped the Mogollon thirty-minute quadrangle at 1:126,720 scale, which contained the Bearwallow Mountain 7.5-minute (1: 24,000) quadrangle. The reconnaissance map depicts four units within the Bearwallow Mountain quadrangle: tuff, basalt, andesite and conglomerate. Unpublished data, collected by Jim Ratte, for production of the New Mexico state geologic map, is integrated into the map. Finally, Senterfit et al. (1996) published a geologic map of Bearwallow Mountain and the adjacent quadrangles for geologic context to their audiomagnetotelluric study of the Bursum caldera.

The primary geologic component mapped in the Bearwallow Mountain quadrangle is the post-caldera basaltic andesite flows of the Bearwallow Mountain Andesite. This report will discuss initial caldera formation, post-caldera collapse breccia deposits and ash-flows, rhyolitic dome formation and eruption, transition to andesitic eruptions, and re-initiation of intra-caldera normal faults during regional extension. Finally, we compare hydrothermal alteration and economic deposits to the Mogollon Mining District.

Geologic Setting

This section discusses the geologic setting, eruption history, and tectonic events of southwestern New Mexico, spatially related to the Bearwallow Mountain quadrangle. The Bearwallow Mountain quadrangle is located in the Mogollon Mountains, a high plateau that acts as the transition zone between the Basin and Range Province to the south and the Colorado Plateau to the north.

Southwestern New Mexico has been the site of numerous compressional and extensional tectonics over the past two billion years. Three major orogenies built the southwestern flank of Laurentia: The Ivanpah orogeny (~1730 Ma) which sutured the Mojave province and the Yavapai province, the Yavapai orogeny (~1800 Ma) accreting arc crust and eventually accreting the Yavapai and Mojave provinces to Laurentia. Finally, the Mazatzal orogeny (1700-1630 Ma) which accreted the Mazatzal province to the Yavapai province (Amato et al., 2008). The order of accretion and exact location of these suture zones is contested because very few outcrops of the rocks exist (Magnani et al., 2004). The Jemez Lineament (under present day Arizona, New Mexico, and Texas) is a Precambrian suture zones, and an intracontinental tectonic and magmatic boundary (Magnani et al., 2004).

The Paleozoic and most of the Mesozoic were relatively inactive and unimportant for the geologic history of the Bearwallow Mountain 7.5-minute quadrangle. No units older than 32 Ma are exposed in and around the quadrangle (Ratte, 1981). The Laramide orogeny ended this quiet period in the late Cretaceous. The Laramide orogeny was a Late Cretaceous to Paleocene event that uplifted the Rocky Mountains in Canada and the United States, and the Sierra Madre Mountains in Mexico (English and Johnston, 2004). Uplift occurred in New Mexico, but later Basin and Range Province and Rio Grande Rift extension obscures most outcrops. Flat-slab subduction, where the subducting plate became more buoyant and the subduction angle decreased, reached thousands of kilometers into the continent, uplifting basement blocks (Saleeby, 2003). Uplift of basement rocks is evident in southwestern New Mexico in the Little and Big Hatchet Mountains, 200 kilometers south of Mogollon (Clinkscales and Lawton, 2017). Subcrops of Paleozoic and Precambrian rocks are found ~ 20 km north of Silver City and throughout southern New Mexico (Clinkscales and Lawton, 2017). Marshak et al. (2000)

attribute this uplift event to re-initiation of Proterozoic extensional faults, creating distinct structural relief. The Laramide orogeny transitioned into extension as the Farallon Plate rolled back at a normal subduction angle (Clinkscales and Lawton, 2017).

The Farallon slab roll back at 36 Ma initiated mid-Tertiary ignimbrite flare-up, and subsequent extension in the western United States, forming three major volcanic fields: Mogollon-Datil Volcanic Field, Sierra Madre Volcanic Field, and San Juan Volcanic Field. Eruption patterns within the MDVF follow those observed in the San Juan volcanic field, and others with initial basaltic andesite to andesite eruptions from 40 Ma to 36 Ma, followed by silicic eruptions and intermittent basaltic flows from 36 Ma to 24 Ma (McIntosh et al., 1992). The MDVF is geographically situated between two areas of bac-arc rifting: the Basin and Range Province to the west, the Rio Grande Rift to the east. The volcanic rocks found within the Bearwallow Mountain quadrangle is within the structural boundary of the Bursum caldera, a 28 Ma collapse structure formed from the eruption of the Bloodgood Canyon Tuff (Ratte, 1981). This eruption occurred during the third episode of the MDVF, and was one of the most voluminous tuff eruption in the volcanic field (1000 km^2; McIntosh et al., 1992). The Apache Springs Tuff then erupted within the caldera depression, depositing 1,200 km^2 of material (McIntosh et al., 1992; Ratte, 1981). Post-collapse resurgent domes and lava flows dominate the quadrangle.

Tertiary Volcanic Rocks

The Bearwallow Mountain quadrangle is primarily comprised of Tertiary volcanic rocks associated with the Mogollon-Datil Volcanic Field. No evidence of older units within the quadrangle, supporting the inferred caldera margin drawn by Ratte (1981) and Senterfit et al.

(1996). The oldest unit observed in the quadrangle is the Apache Springs Tuff and the youngest volcanic unit is the Bearwallow Mountain Andesite (Table 1). This section, discusses the volcanic stratigraphy and the observed relations between units (see appendix for detailed unit descriptions).

The Apache Springs Tuff (**Tas**) is the oldest observed unit in the quadrangle. Tas is comprised of layered ash-flow tuffs, tuffaceous conglomerates, and brecciated flows associated with intra-caldera fill. The reported age of the Apache Springs Tuff is 27.9 Ma, immediately following the eruption of Bloodgood Canyon Tuff at 28.0 Ma (McIntosh et al., 1992). The structural extent of the Bursum caldera uses the spatial distribution of Apache Springs Tuff (Ratte, 1981).

The Fanney Rhyolite (**Tf**) is stratigraphically above Tas and below Mineral Creek Andesite in the Bearwallow Mountain quadrangle. Tf consists of intrusive and extrusive rhyolite domes and lavas. It the first major erupted product after the collapse of the Bursum caldera, implying a 1.5-million-year hiatus in magmatism. Fanney Rhyolite is prominent in the Mogollon and Holt Mountain quadrangles and is present both within and outside the inferred caldera margin (Ratte, 1981; Ratte et al., 2006).

The Mineral Creek Andesite (**Tmc**) erupted after Tf along the western margin of the caldera. The Tmc is only observed as thin lavas within the Bursum caldera in Mineral Creek. In some cases, Tmc is stratigraphically below Tf implying a duel eruptive event. Tmc is older than the two other andesites in the region (Last Chance Andesite and Bearwallow Mountain Andesite) and is stratigraphically below the Deadwood member of Fanney Rhyolite (Tfd).

The Willow Creek Latite (**Twl**) is stratigraphically above Tf and below Tba. There is only a small outcrop of Twl near Indian Tank on the southeastern corner of the quadrangle. Ratte

and Gaskill (1975) originally described the Twl, and these authors interpreted the unit as dome complexes related to the Bursum caldera. More mafic facies of Twl are found in the neighboring Negrito Mountain quadrangle (M. Zimmerer, written commun., 2019). The apparent thickness of Twl is around 100 feet, thickening to the east, and does not outcrop farther west. No age date is available for the unit.

First described by Ferguson (1927), the Deadwood member of the Fanney Rhyolite (**Tfd**) is the pyroclastic facies of Fanney Rhyolite. The unit has not been dated, and field observations suggest that it is younger than both Tf and Tmc, but older than Tlc and Tba. The Tfd is found in the southern third of the quadrangle, with significant outcrops along Mineral Creek, above Tf near Route 159, and along the upper reaches of Copper Creek. In most places, Tfd appears to be no more than 400 feet thick due to erosion. Along Mineral Creek, the apparent thickness is more than 1,000 feet. The unit pinches out to the west and east suggesting the eruption location was within the quadrangle, but a vent location is unknown.

Last Chance Andesite (**Tlc**) is comprised of aphanitic lava flows above Tfd and unconformabley below Dog Gulch Conglomerate and Bearwallow Mountain Andesite. Tlc is indistinguishable from Tmc in the field unless Tfd is present. Ratte (1981) reported the K-Ar age between 25.0 ± 0.6 million years and 23.2 ± 0.6 million years. Tlc is found along the western edge of the quadrangle, above Tfd.

Bearwallow Mountain Andesite (**Tba**) is the dominant unit in the quadrangle. It covers the northern two-thirds of the quadrangle, and caps some of the southern ridges. The distribution of Tba indicates that the entire quadrangle was covered with the unit until later erosion exposed older rocks. Tba is a dark grey vesicular aphanitic basaltic andesite. Some sequences contain small olivine, but the flows are overall crystal-poor (O'Dowd, 2018). Bearwallow Mountain is a

suggested vent location for this unit as it thins in all directions from the peak. Willow Creek (southeastern corner of the quadrangle) exposes ~400 feet of Bearwallow Mountain Andesite, which suggests that the unit covered the entire quadrangle prior to erosion. Small windows along Copper Creek expose lower units (Fanney Rhyolite and Deadwood Member) signifying a paleo-topographic high. McIntosh and Chamberlin (1994) estimated the age of the Bearwallow Mountain Andesite to be 26.1 Ma.

Geochemistry

Previous studies presented whole-rock geochemistry of the units found in the Bearwallow Mountain quadrangle. These data are summarized from Salings (2017) and O'Dowd (2018) and presented in Figures 1 and 2. These data were broken into units where possible, or grouped by composition. Whole-rock geochemistry illustrates the compositional differences between the andesites in the region from the more silica-rich rhyolites and tuffs. The FeO_T vs. SiO_2 shows a significant difference in iron content between the andesites and rhyolites. Most Tba samples have FeO_T around 10% while Tf, Tas, and other rhyolites have FeO_T around 2%. Furthermore, Tba, Tmc, and Dacite of Spurgeon Mesa (in the adjacent Mogollon and Alma quadrangles) have high Sr concentrations, while Tf, Tas, and other rhyolites have lower Sr concentrations. Finally, La contents show little correlation with silica content, rather every sample ranges between 20 and 60 ppm.

Units within the Bearwallow Mountain quadrangle generally fall into two categories: high-silica rhyolites and tuffs, and low-silica andesites (Figures 1 and 2). The andesites typically have higher FeO and Sr contents, while the rhyolites and tuffs have higher potassium contents. Further geochemical analyses is required to differentiate individual phases within each unit,

namely the Fanney rhyolite and the Deadwood member of the Fanney rhyolite. For more detailed geochemical analyses on the Bearwallow Mountain andesite, see O'Dowd (2018). For further information on the Apache Springs tuff, see Sailings (2017).

Structure

Structure in and around the Bearwallow Mountain quadrangle is complicated by over-printing and reactivation of structures recorded over the past 1.5 billion years and collapse of the Burusm caldera. Structures north of the Bearwallow Mountain quadrangle follow the orientations of Precambrian suture zones (Ratte, 2001). These structures follow the Morenci-Reserve fault system, which is distinct from the San Agustin trend (Houser, 1994). This long-lived fault system traces southwest to Sonora, Mexico, and was active between 30 Ma to the Pleistocene. The Mangas graben and associated faults follow the orientation of Laramide compression with deformation commencing around 19 Ma (Houser, 1994). This fault system exposed the margin of the Bursum caldera in the Mogollon and Holt Mountain quadrangles.

Normal faults to the southwest of Mogollon have a different orientation than those found just west (Alma Basin) and northeast (Morenci-Reserve Fault Zone). These structures south of Mogollon trend NW-SE as they bend around the Mogollon Plateau and merge with Rio Grande Rift structures near Las Cruces, NM (Figure 3). Basins in SE Arizona follow this same orientation. This orientation is indicative of the earlier compressional regimes of the Laramide deformation event and the Jurassic Mexican Borderland Continental rift system (Lawton and McMillan, 1999). Both of these events followed similar orientations, and created weak lineaments influencing Tertiary extension. No major basins opened in the Mogollon Plateau, though there are smaller disconnected basins near Gila Cliff Dwellings National Monument

(Figure 4). The structures within the Bearwallow Mountain quadrangle represent a transition between N-S Mangas graben structures and E-W structures of the Jurassic and Paleocene tectonic regimes. The Bearwallow Mountain quadrangle is dominated by a central graben. E-W faults bound Mineral Creek in the south-central region of the quadrangle, but then converge to the east. Smaller N-S faults intersect these E-W faults, especially near Cooney Peak and Sandy Point. No faults cut Bearwallow Mountain Andesite, but some can be inferred based on surrounding lithology. This implies that extension in the quadrangle is older than Bearwallow Mountain Andesite (25-22 Ma), and therefore, unrelated to the Mangas graben formation. The bi-directional stress is consistent with the Mogollon and Holt Mountain quadrangles, representing different phases of extension. The N-S structures in these quadrangles are most likely related to the Mangas graben, while the NW-SE faults are related to older reactivated reverse faults. It is impossible to state whether the structures observed in the quadrangle are purely tectonic or caldera-related. In practice, it is likely that the structures are a combination of both systems.

Geophysics

Several geophysical studies have focused on the Bursum Caldera and the surrounding volcanic field (Schneider and Keller, 1994; Senterfit et al., 1996). Senterfit et. al. (1996) found that the western margin of the Bursum caldera is electrically conductive presumably due to the presences of water and sulfide-rich hydrothermal veins. The Bearwallow Mountain Andesite conceals the northern margin of the caldera, but Senterfit et al. (1996) suggest a zone of conductivity similar to the western margin that could be the caldera fracture system. These authors traced the margin between Bearwallow Mountain and Corner Mountain in the

Bearwallow Mountain quadrangle (Figures 5 and 6). Figure 6 shows the reinterpreted AMT models through the western margin of the caldera and the northern margin from Senterfit et al. (1996). Lines 1 through 3 show TM mode and 1D models through the western margin of the caldera while lines 4 and 5 show TM mode and 1D models through the inferred northern margin. In theory, the caldera margin should be an area of low resistivity due to more fractures and faults, while more solid rock will be more resistive. Lines 1 and 2 clearly show low restive regions on the left side of the profile, and line 3 shows a broader low resistive region. These three low restive areas can be correlated to the north-south trending caldera margin. The northern margin is more ambiguous, probably because and faults and fractures are buried under hundreds of meters of more recent basaltic andesite. Lines 4 and 5 show pockets of low restive zones in the middle of line 4. This line of reasoning is only sound if we assume that the faults along the western margin are remnants the caldera, and not more recent features related to the Mangas trench formation.

Schneider and Keller (1994) did a broad gravity study of the Colorado Plateau – Basin and Range Province margin in southwestern New Mexico. They placed the margin between Silver City, NM and Datil, NM based on evidence for thickening crust. We reinterpreted their original gravity data and made an isostatic gravity map of the Bursum caldera region (Figure 7). The isostatic residual method removes signals deeper than 25 to 30 kilometers, therefore represents density variations in the upper crust. High gravitational signals are seen along the western margin of the Bursum caldera in the Mogollon quadrangle, and along the Morenci-Reserve fault system. Additional highs correspond to the southern margin of the caldera, southeast of the Holt Mountain quadrangle. These signals follow the NW-SE trend of Basin and Range extension. Gravitational lows are found within the center of the inferred margin of the

caldera, and northeast of the Bearwallow Mountain quadrangle. There appears to be no gravitational change along the northern margin of the inferred caldera. The gravity lows north of the Bursum caldera do not seem to correspond to any other inferred caldera structure. The older Gila Cliff Dwellings caldera, east of the Bursum caldera, does not have similar low signatures as observed with the lows of the Bursum caldera. Likewise, to the west, the Mogollon caldera has no obvious lows.

These geophysical surveys allow us to interpret near surface and upper crustal bodies associated with the Bursum caldera. Though there is no surficial evidence for the northern caldera margin, these geophysical surveys allow us to infer a margin between Bearwallow Mountain and Corner Mountain. Furthermore, we can also infer a large silicic upper crustal body that likely fed the ash-flow tuff eruptions of the Bursum caldera around 28 million years ago.

References

Amato, J. M., Boullion, A. O., Serna, A. E., Farmer, G. L., Gehrels, G. E., and Wooden, J. L., 2008, Evolution of the Mazatzal province and the timing of the Mazatzal orogeny: Insights from U-Pb geochronology and geochemistry of igneous and metasedimentry rocks in southern New Mexico: GSA Bulletin, v. 120, no. 3/4, p. 328-346.

Bikerman, M., Bell, K., and Card, J. W., 1992, Strontium and neodymium isotopic study of the Western Mogollon-Datil Volcanic region, New Mexico, USA: Contributions to Mineralogy and Petrology v. 109, p. 459-470.

Cather, S. M., 1989, Post-Laramide Tectonic and Volcanic Transition in West-Central New Mexico: New Mexico Geological Society Guidebook, p. 91-97.

Clinkscales, C. A., and Lawton, T. F., 2017, Mesozoic-Paleogene Structural Evolution of the Southwestern U.S. Cordilla as Revealed in the Little and Big Hatchet Mountains, Southwest New Mexico, USA: Geosphere, v. 14, no. 1, p. 162-186.

Elston, W. E., 1976, Volcano-tectonic control of ore deposits, southwestern New Mexico: New Mexico Geological Society Guidebook, v. 21, p. 174-153.

English, J. M., and Johnston, S. T., 2004, The laramide orogeny: what were the driving forces?: International Geology Review, v. 46, p. 833-838.

Ferguson, H. G., 1927, Geology and Ore Deposits of the Mogollon Mining District, New Mexico: USGS Bulletin 787.

Houser, B. B., 1994, Geology of the late Cenozoic Alma Basin, New Mexico and Arizona: New Mexico Geological Society Guidebook, v. 45, p. 121-124.

Houser, B. B., 1987, Geologic map of the Alma quadrangle, Catron County, New Mexico: US Geological Survey, scale 1:24,000.

Lawton, T. F., and McMillan, N. J., 1999, Arc Abandonment as a Cause for Passive Continental Rifting: Comparison of the Jurassic Mexican Borderland rift and Cenozoic Rio Grande Rift: Geology, v. 27, no. 9, p. 779-782.

Magnani, M. B., Miller, K. C., Levander, A., and Karlstrom, K., 2004, The Yavapai-Mazatzal boundary: A long-lived tectonic element in the lithosphere of southwestern North America: GSA Bulletin, v. 116, no. 7/8, p. 1137-1142.

Marshak, S., Karlstrom, K., and Timmons, J. M., 2000, Inversion of Proterazoic extensional faults: an explanation for the pattern of Laramide and Ancestral Rockies intracratonic deformation, United States: Geology, v. 28, no. 8, p. 735-738.

McIntosh, W. C., Chapin, C. E., Ratte, J. C., and Sutter, J. F., 1992, Time-stratigraphic framework for the Eocene-Oligocene Mogollon-Datil Volcanic Field, Southwest New Mexico: Geological Society of America Bulletin, v. 104.

McIntosh, W. C., and Chamberlin, R.M., 1994, $^{40}Ar/^{39}Ar$ geochronology of middle to late Cenozoic ignimbrites, mafic lavas, and volcanoclastic rocks in the Quemado region, New Mexico: New Mexico Geological Society Guidebook, v. 45, p. 165-185.

Ratte, J. C., 2001, Geologic map of the Tularosa Mountains 30' X 60' quadrangle, Catron County, New Mexico: U.S. Geological Survey.

Ratte, J. C., and Gaskill, D. L., 1975, Reconnaissance geologic map of the Gila Wilderness study area, southwestern New Mexico, 886.

Ratte, J. C., 1981, Geologic map of the Mogollon quadrangle, Catron County, New Mexico, 1557.

Ratte, J. C., Lynch, S., and McIntosh, W. C., 2006, Preliminary geologic map of the Holt Mountain quadrangle, Catron County, New Mexico: New Mexico Bureau of Geology and Mineral Resources, OFGM 120.

Saleeby, J., 2003, Segmentation of the laramide Slab - evidence from the southern Sierra Nevada region: GSA Bulletin, v. 115, no. 6, p. 655-668.

Schneider, R. V., and Keller, G. R., 1994, Crustal structure of the western margin of the Rio Grande rift and Mogollon-Datil volcanic field, southwestern New Mexico and southeastern Arizona: Geological Society of America Special Paper, v. 291, p. 207-226.

Senterfit, R. M., Ratte, J. C., Kamilli, R. J., and Klein, D. P., 1996, Audiomagnetotelluric study of the Bursum Caldera and the Mogollon mining District, Southwest New Mexico: U.S. Geological Survey.

Weber, R. H., and Willard, M. E., 1959, Reconnaissance geologic map of the Mogollon thirty-minute quadrangle: New Mexico Bureau of Mines and Mineral Resources, scale 1:126,720.

Table 1. Geochronology and methods of units found in the Bearwallow Mountain quadrangle

Unit	Method	Age	Error	# Analyses	Source
Tas	$^{40}Ar/^{39}Ar$	27.98	0.09	3	McIntosh et al. (1992)
Tbc	$^{40}Ar/^{39}Ar$	28.05	0.04	8	McIntosh et al. (1992)
Tf	K-Ar	26-24.4	?	2	Bikerman et al. (1992)
Tmc	Whole-rock K-Ar	25	0.5	?	Strangway et al. (1976)
Tlc	Whole-rock K-Ar	25-23.2	0.6	?	Ratte (1981)
Tba	$^{40}Ar/^{39}Ar$	26.1	?	?	McIntosh and Chamberlin (1994)

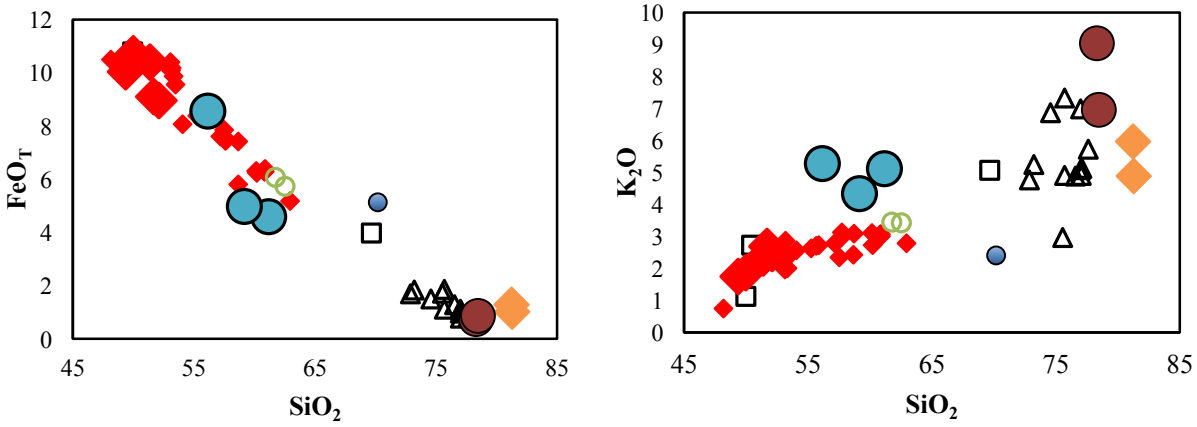

Figure 1: FeO_T and K_2O over SiO_2, respectively. Red diamonds are Bearwallow Mountain andesite, blue circles are Mineral Creek andesite, green diamonds are Apache Springs tuff, brown circles are Fanney rhyolite, white triangles are rhyolites, white circles are Dacite of Spurgeon Mesa, and white squares are dikes.

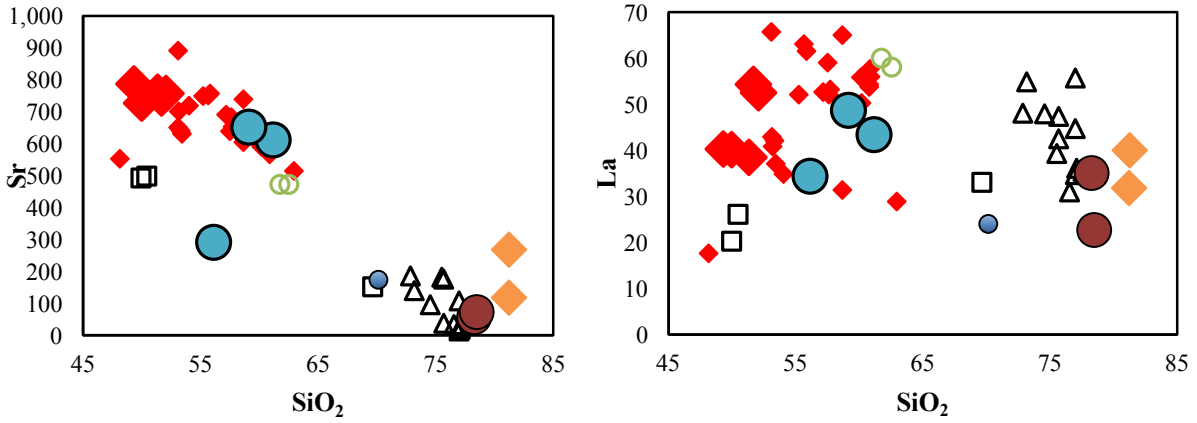

Figure 2: Sr and La (ppm) over SiO_2 (wt. %) , respectively. Red diamonds are Bearwallow Mountain andesite, blue circles are Mineral Creek andesite, green diamonds are Apache Springs tuff, brown circles are Fanney rhyolite, white triangles are rhyolites, white circles are Dacite of Spurgeon Mesa, and white squares are dikes.

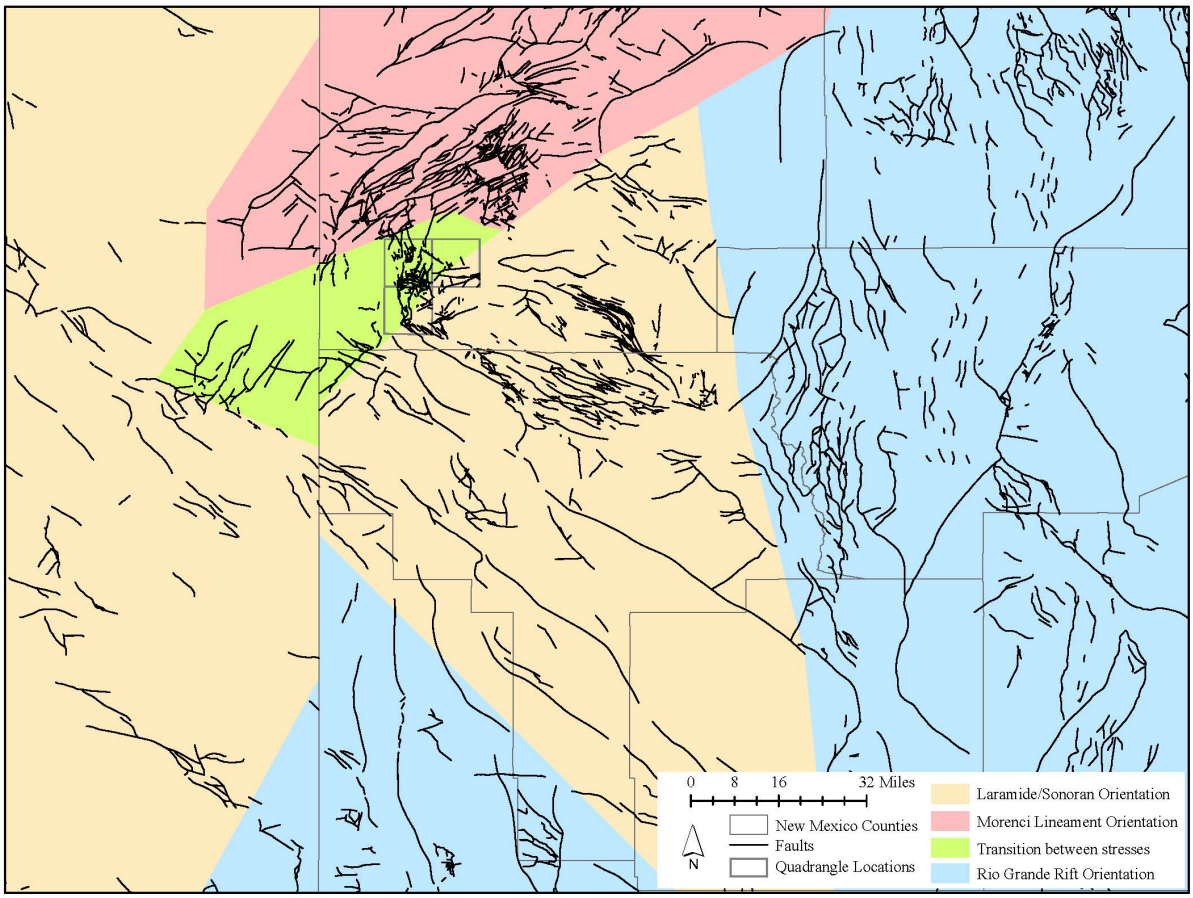

Figure 3: Stress regimes of SW New Mexico. Orange is southern Basin and Range extension with faults trending NW-SE (~30 Ma to ~5 Ma). Blue represents N-S trending faults associated with Rio Grande Rifting (32 Ma to present). Red represents NE-SW trending faults associated with the Morenci-Reserve Fault Zone.

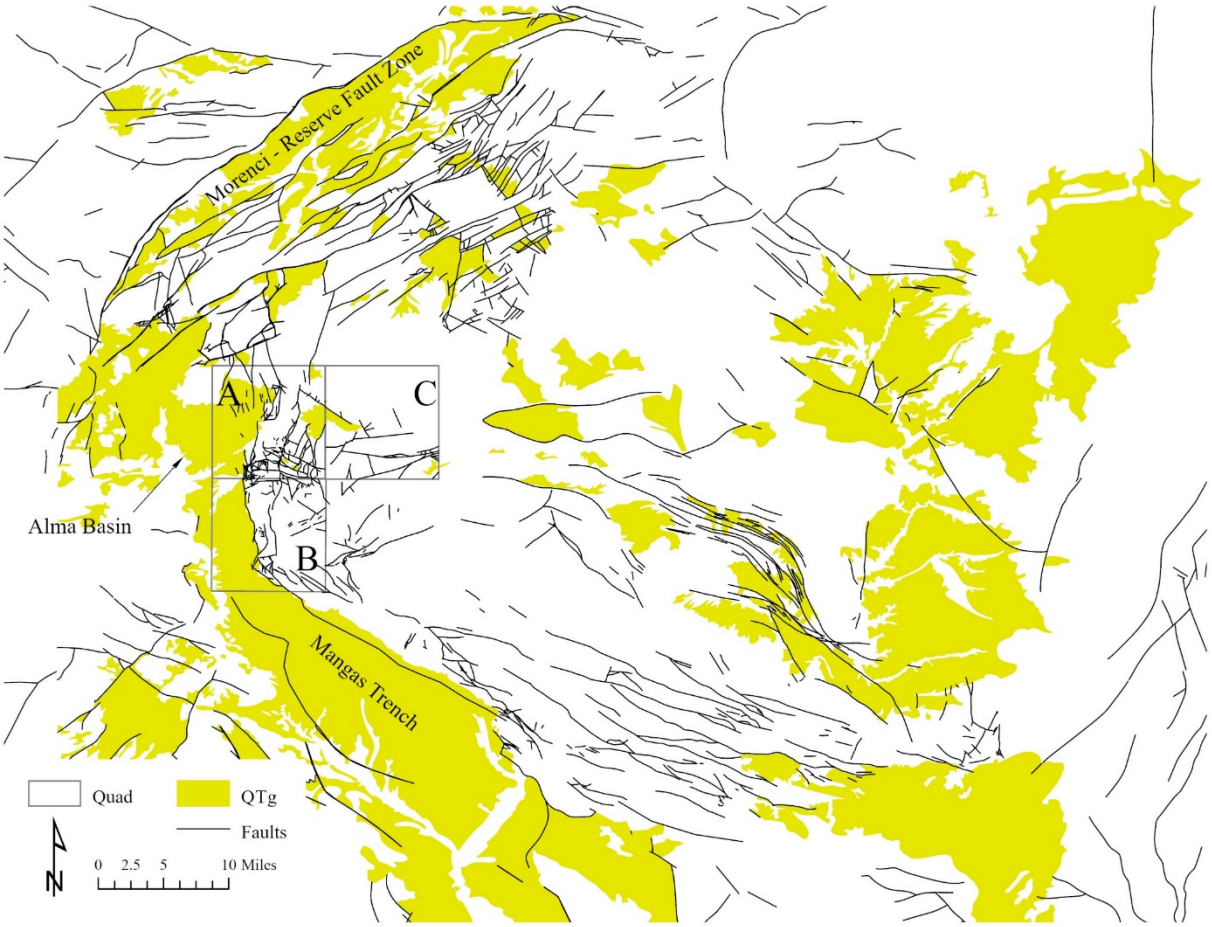

Figure 4: Oligocene to Pleistocene basins in the Mogollon Mountains. The Alma Basin (west of the Mogollon quadrangle) represents the transition between Morenci-Reserve fault system and the Mangas trench. This basin system opened around 19 million years. A: Mogollon quadrangle, B: Holt Mountain quadrangle, C: Bearwallow Mountain quadrangle.

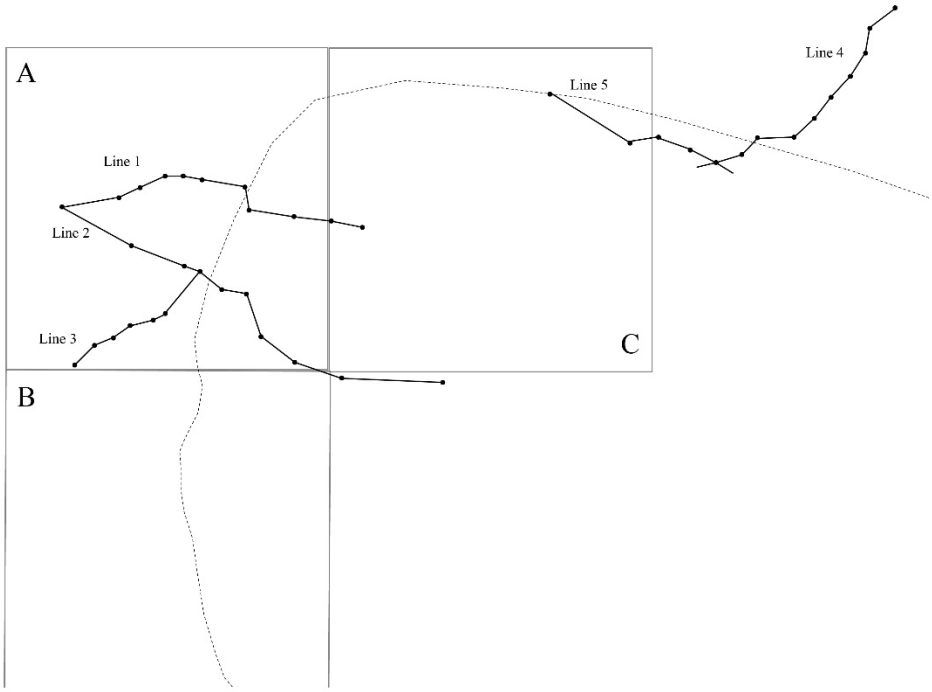

Figure 5: Reference map with quadrangles (A: Mogollon, B: Holt Mountain, C: Bearwallow Mountain), inferred caldera margin (dotted line), and AMT surveys from Senterfit, et al. (1996). The next page shows TM mode and 1D models for each line.

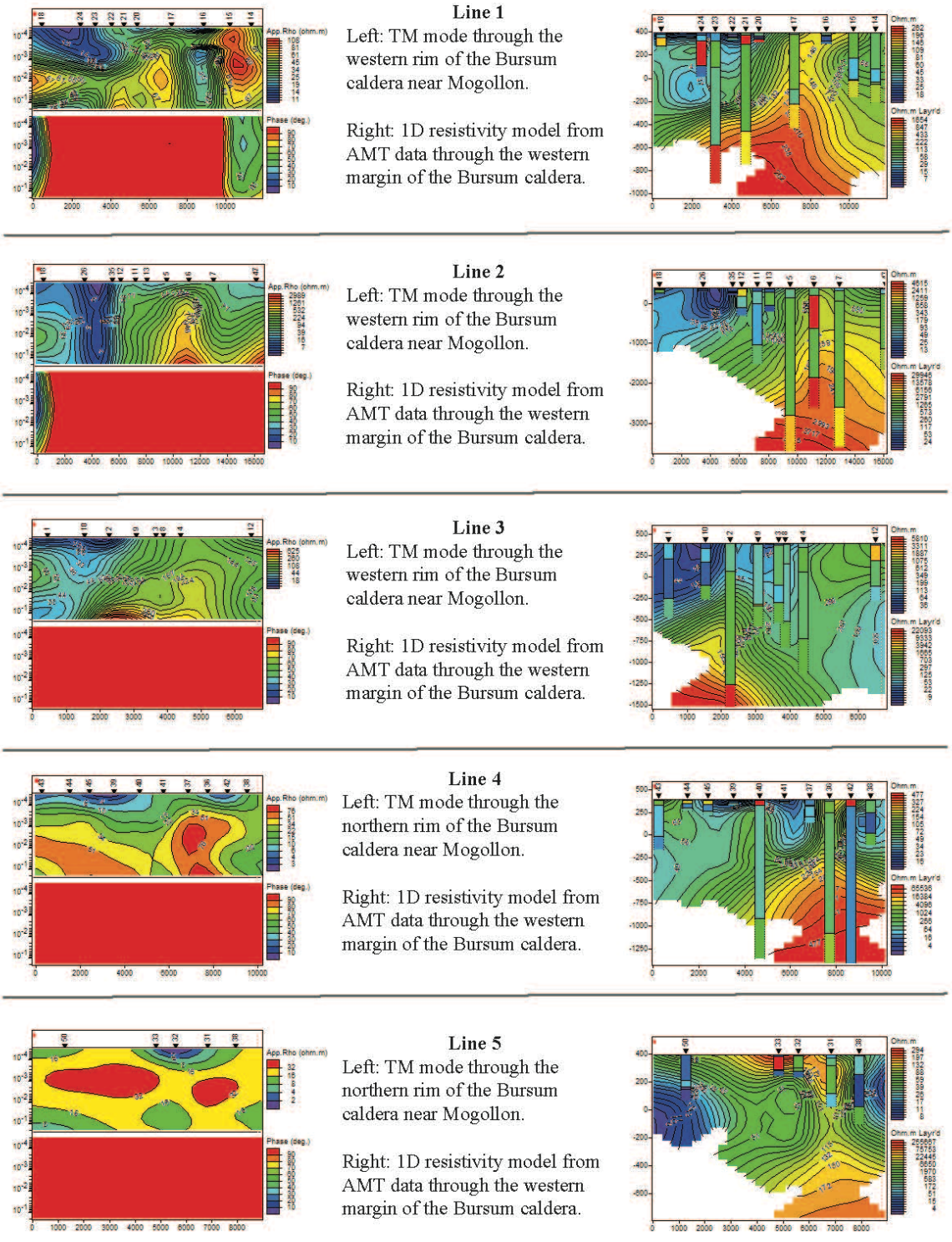

Figure 6: Composite of TM mode data (left figures) and one-dimensional inversion modeling of the TM mode AMT data (right figures) across the Bursum caldera margin. The location of the profiles are shown in Figure 6. The triangles with numbers are the location of the AMT stations. The columns are the one-dimensional models are the actual model.

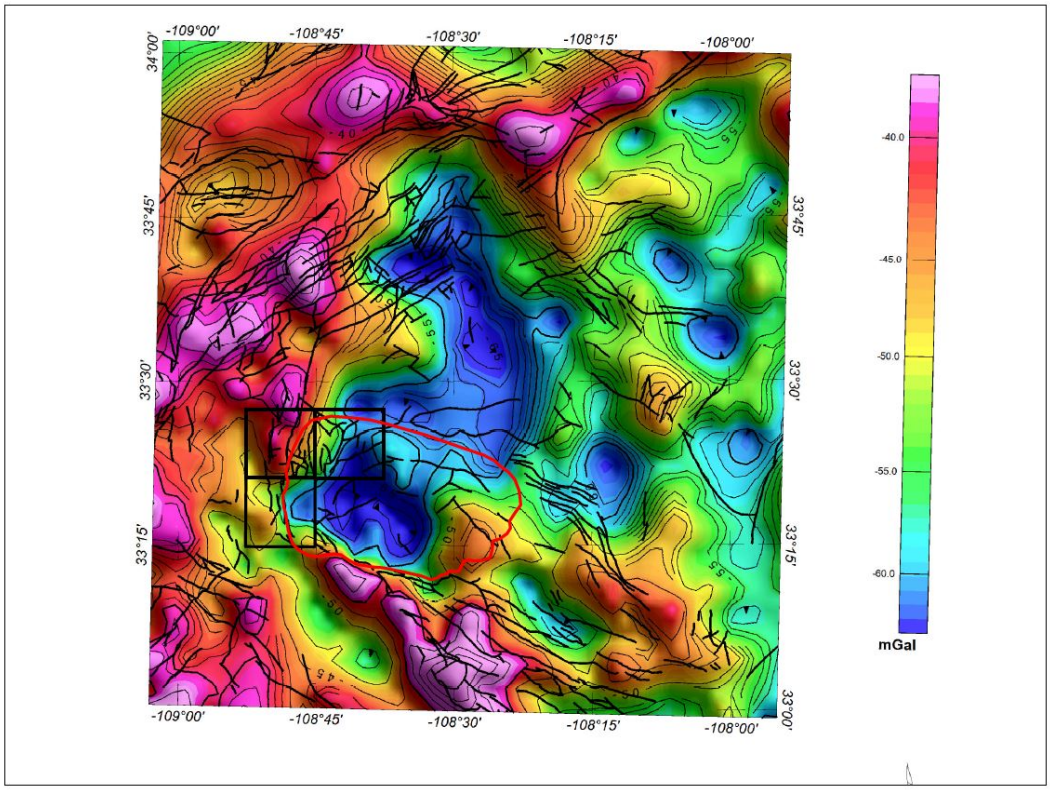

Figure 7: Isostatic residual gravity anomaly map of Bursum caldera and the vicinity. The three black boxes are the Bearwallow Mountain quadrangle (top right), Mogollon quadrangle (top right), and Holt Mountain quadrangle (bottom left). The red line is the inferred margin of the Bursum caldera (Senterfit et. al., 1996), and the black lines are faults.

MANUSCRIPT 2: VLF-EM AND MAGNETIC ANALYSIS OF THE CONSOLIDATED MINE SITE, MOGOLLON MINING DISTRICT, NEW MEXICO

Abstract

The Mogollon Mining District is a volcanic-epithermal silver-gold deposit hosted in mid-Tertiary volcanic rocks of the Mogollon-Datil Volcanic Field in southwestern New Mexico. first discovered in the late 1880's, silver and gold production continued until the 1940's. Exploration efforts in the 1980's and 2010's have been concentrated along the Queen Vein, north of the town of Mogollon.

VLF-EM and magnetic data were used to create a series of VLF-EM and magnetic anomaly maps and VLF-EM two-dimensional models. These data, combined with old geology and mine data, to identify possible buried veins. Such analyses can both improve the known geology of the district, but also may provide more targets for exploration. The magnetic and VLF-EM analyses suggest the presence of a vertical conductor along the Independence vein. Our results also suggest the presence of another fault splaying off the Queen vein to the east. Both structures are good targets for future exploration.

Introduction

The Mogollon Mining District, situated in southwestern New Mexico (Figure 1), is the most profitable volcanic-epithermal ore deposit in New Mexico, producing more than 20 million ounces of silver and 300,000 ounces of gold over its 40 year production history (McLemore, 1994). For this reason, the structure, mineralogy, and economic geology of the area is known in detail (Anderson, 1939; Bornhorst and Kent, 1985; Bornhorst et al., 1984; Eveleth, 1979; Ferguson, 1927; Hiner, 2016; Ratte, 1975, 1981; Ratté et al., 1984; Senterfit et al., 1996). This district lies along the western margin of the Bursum caldera (Ratte, 1981), though the structures are likely due to more recent extension (Houser, 1994).

Sergeant James Cooney (Anderson, 1939; Hiner, 2016) discovered gold and silver in the Mogollon Mining District in the late 19th century. By 1890, at least four mines – Little Fanney,

Confidence, Maud S, and Cooney – were operating within the district, and peak production occurred in 1914 with 1,400,000 ounces of silver and 30,000 ounces of gold being produced (Hiner, 2016). Early geologists noted that the Queen vein, following the Queen fault, seemed to be a conduit of hydrothermal fluids (Ferguson, 1927). Descriptions the ore hosted rocks suggest emplacement as emplaced as low sulfidation epithermal deposits due to the predominant vein-hosted mineralization, high silver content and mineral assemblages (Anderson, 1939; Ferguson, 1927; Hiner, 2016).

Very low frequency electromagnetic (VLF-EM) and magnetic data, collected in June 2019, characterize the structures and to locate possible veins near the planned Consolidated Mine. The magnetic and VLF-EM data were analyzed using mapping methods and the VLF-EM data were modeled using Fraser and K-H filters and the two-dimensional (2D) inversion of the Fraser data. These maps and models present a better understanding of the structure of veins and the location of conductive minerals. Additionally, the results identify new targets for exploration, and improve our understanding of the bedrock geology.

Background

Geologic Background. Volcanic rocks related to the mid-Tertiary ignimbrite flare-up (McIntosh et al., 1992) dominate the geology of the Mogollon Mining District (Ratte, 1981). McIntosh et al. (1992) separated the volcanic rocks into four distinct episodes: Episode 1 took place from 37 Ma to 33 Ma, Episode 2 occurred from 33 Ma to 31 Ma, Episode 3 erupted from 29 Ma to 27 Ma, and Episode 4 erupted from 26 Ma to 24 Ma. These episodic eruptions were seen throughout New Mexico and Arizona, and may have been caused by slab rollback of the Farallon plate after Laramide deformation (Clinkscales and Lawton, 2017). After the ignimbrite

flare-up, volcanism transitioned back to andesite and basaltic andesite composition lavas around ~25 Ma (McIntosh et al., 1992). This later series is evident in the stratigraphy of the Mogollon area as described by Ferguson (1927) and Ratte (1975). The youngest volcanic eruption in the Mogollon region is the Bearwallow Mountain Formation which erupted between 25 and 22 Ma (Ratte, 1975) though younger rift basalts are present in other parts of the Mogollon-Datil Volcanic Field (MDVF).

The volcanic units within the Mogollon Mining District result from the eruption, collapse, and subsequent resurgence of the Bursum caldera (Ratte, 1981). The Bursum caldera collapsed around 28 Ma with the eruption of the Bloodgood Canyon Tuff (McIntosh et al., 1992). Bimodal andesite and rhyolite domes, and lava flows exploited and erupted along the ring fractures of the caldera, producing large volumes of material. The Mogollon Mining District is situated along the inferred structural margin of the caldera, and is comprised almost entirely of these resurgent lava flows and domes. The important units related to the ore geology are the Fanney rhyolite, Mineral Creek andesite, and Last Chance andesite.

The Fanney rhyolite was one of the first resurgent units erupted after the collapse of the caldera. Several locations in the district have examples of the intrusive component of the Fanney rhyolite, suggesting that it exploited the ring fractures (Ratte, 1975, 1981). The Mineral Creek Andesite and Last Chance Andesite are both aphanitic lava flows and are indistinguishable from each other except when the Deadwood member of the Fanney rhyolite is present between them (Ratte, 1981).

Ore Deposit Styles and Alteration. There are few studies on the post-eruption hydrothermal alteration within the Mogollon Mining District. Ferguson (1927) noted that the mineralized veins are steeply dipping, striking N/S and WNW/ESE, with the WNW/ESE veins

hosting more precious metals than the N/S trending veins. Early geologists also noted that the Queen vein, following the Queen fault, seemed to be the conduit of the hydrothermal fluids, however, it contained small amounts of gold and silver (Ferguson, 1927). Ferguson (1927) also noted that most of the ore was found where the vein cut both the Fanney rhyolite and Mineral Creek andesite, and was rare adjacent to other units.

Argillic, silicic, sericitic, and propylitic host rock alteration occurs alongside hydrothermal veins in varying degrees depending on the type of rock (McLemore, 1994). The Mineral Creek andesite is severely altered throughout the district while the Fanney rhyolite is only locally altered (Bornhorst and Kent, 1985). Trace element geochemistry suggests that the addition of Rb and K to both wall rocks during alteration, and Na, Sr, and Ca were mostly removed (Bornhorst and Kent, 1985).

Bornhorst (1984) found that fluids responsible for mineralization within the Mogollon Mining District emplaced at temperatures between 180 ˚C and 270 ˚C (Figure 2). Quartz precipitated at the highest temperature, while fluorite precipitated at the lowest temperature (Figure 2). Emplacement of veins occurred in four stages.. The first stage was a high temperature (~ 260 ˚C) quartz stage, followed by a slightly lower temperature (240 ˚C) calcite stage. Stage III precipitated calcite and quartz between ~ 240 ˚C and ~210 ˚C. Finally, precipitation of fluorite occurred between 200 ˚C and 160 ˚C. Precious metals deposits do not occur outside with the quartz mineralization, suggesting the main economic mineralization phase occurred earlier in the hydrothermal series, and was then over-printed by later calcite and fluorite veins (Bornhorst and Kent, 1985; Bornhorst et al., 1984; Ferguson, 1927). Finally, a supergene enrichment stage occurred after mineralization, helping to concentrate precious metals (Ferguson, 1927).

Regional Geophysics. The Mogollon Mining District and surrounding region has been the focus of only a handful of geophysical studies, primarily related to the deep crustal structure (Schneider and Keller, 1994) and investigations into the buried Bursum caldera margin (Senterfit and Abrams, 1991; Abrams, et al., 1992; Senterfit et al., 1996). This region is unique because it is unaffected by the Rio Grande Rift to the east and Basin and Range to the west, and extension seems to wrap around the bulk of the Mogollon Plateau (Elston, 1976). An isostatic residual gravity anomaly map (Figure 3) shows density variations in the upper crust near the Mogollon Mining District. The district lies on the boundary between higher gravity to the west and lower gravity to the east. The denser crust may be related to denser Precambrian crust compared to the less dense mid-Tertiary crust to the east. More localized isostatic residual gravity anomalies of the Mogollon Mining District and the surrounding area show a large gravity minima to the east and northeast of this study area. This anomaly aligns with the Bursum caldera (outlined in red) but there is no explanation for the rest of the anomaly, but is probably related to the volcanic units.

Regional magnetic anomalies are show maxima south of the Mogollon mining District, and minima north (Figure 4). The anomalies are more randomly spaced than the isostatic residual gravity anomalies because the magnetic susceptibility of the surface volcanic rocks probably varies widely within these units.

Geophysics

Geophysical Data Collection. A GEM GSM-19T magnetometer and VLF-EM receiver were used for data collection along the major veins within the Mogollon Mining District (Figure 5). The GSM-19T is a portable proton magnetometer with a 0.15 nT sensitivity where the data were collected at one reading per second. A one reading per second rate was used to allow

constant reading while walking. The meter recorded magnetic field strength in nanoTeslas (nT) along with GPS location (latitude and longitude) and elevation data. The VLF-EM readings used the 25.2 kHz signal from La Moure, North Dakota. Signals from Cutler, Maine (24.0 kHz) and Jim Creek, Washington (25.8 kHz) were attempted but were too weak. The VLF-EM data storage for the magnetic and VLF-EM readings is automatic. The magnetic data were collected in a random grid pattern, while the VLF-EM data were collected along parallel lines.

VLF-EM and Magnetic Data. The VLF-EM and magnetic data were collected in the area surrounding the Consolidated Mine Site in the Mogollon Mining District. Figure 5 shows the data point distribution of total-field magnetic stations, while Figure 5 shows the data distribution of VLF-EM stations. The VLF-EM data were collected in a 20-meter spacing, while the magnetic data were collected in a 1-second continuous interval along each path. The northwest portion of the maps are represented by only one line of data, while the southeast has a higher density of points. Parallel lines were attempted, but thick brush and cliffs made this task difficult.

VLF-EM and Magnetic Anomaly Map Analysis. IP (in-phase) VLF-EM, OP (out-of-phase) VLF-EM, Hilbert transformed VLF-EM, and total-field magnetic anomaly maps were produced from data collected in the study area in 2019 (Figure 5).

IP VLF-EM Anomaly Map. Data collected in 2019 was gridded using a 20-meter spacing to produce an IP VLF-EM map in Figure 7. The IP VLF-EM anomaly map shows the southeastern portion of the map as a conductivity maxima, but is too broad to correlate it to any one fault. A conductivity minima is associated with the NW trending Independence fault, while a maxima is associated with offshoots of the Ida May fault to the south. These conductivity minima and maxima do not correlate to the known structures as well as the magnetic anomaly

map (Figure 6). The anomaly map indicates that the Graveyard Fault is the most conductive in the study area, followed by portions of the Queen fault.

OP VLF-EM Anomaly Map. The same parameters were used from the IP VLF-EM anomaly map to make an OP VLF-EM anomaly map. Figure 8 shows the OP VLF-EM anomaly map. A conductivity minima is in the southeastern corner of the map and trends NE-SW. Additionally, a conductivity maxima is located along the Fanney fault in the southwestern corner of the map. These bodies are broad and similar in fashion to the IP VLF-EM anomalies in Figure 7.

IP VLF-EM Hilbert Transform. The IP and OP phases of the VLF-EM data were passed through a Hilbert transform to create a Hilbert transform VLF-EM anomaly map (Figure 8). The Hilbert transform is a phase shifter that aligns the IP and OP VLF-EM signal over the inferred source, thereby an anomaly map easier to interpret. The Hilbert transform is:

$$H(x) = \frac{1}{\pi}\int_0^{\infty} [IF(\omega)\cos(\omega x) - RF(\omega)\sin(\omega x)]d\omega$$

where RF and IF are the real and imaginary components of the VLF-EM data (Thomas, 1969).

The anomaly map shows conductivity maximas that align with known structures than either the IP VLF-EM (Figure 7) or the OP VLF-EM (Figure 8) anomaly maps. One linear conductivity maxima follow the NW trace of the Independence fault (Area 2 in Figure 9) while another is oriented E-W and crosscuts the Graveyard fault and the Queen fault (Area 1 in Figure 9). Finally, a large conductivity maxima trends NE from the intersection of the Queen and Socorro faults and crosscuts the Graveyard fault (Area 3 in Figure 9). Conductivity minima bound the NE trending maxima to the SE and to a lesser extent to the NW.

Total-field Magnetic Anomaly Map. A total-field magnetic anomaly map was produced using 20-meter grid spacing (Figure 6). The magnetic anomalies show similar patterns as the Hilbert transformed VLF-EM anomaly map (Figure 9). There is a distinct NW-SE trend of a magnetic boundary between magnetic maxima to the north and magnetic minima to the south of the Independence fault. Another magnetic maxima is located along the Queen vein near the intersection of the Socorro fault, and follows the same trend as the Hilbert transformed anomaly in Area 3 (Figure 8). Magnetic minima are found along the Fanney fault and the southern portion of the Queen fault.

VLF-EM Fraser Filtered Data Analysis. The Fraser filter method was developed by Fraser (1969) to shift IP and OP VLF-EM readings over the inferred source, while removing signal noise that affected the ability to interpret the data. The Fraser filter is produced using the following equation:

$$\left(\frac{\Delta Z}{2\pi}\right) Ix \left(\frac{\Delta x}{2}\right) = -0.205H_{-2} + 0.323H_{-1} - 1.446H_0 + 1.446H_1 - 0.323H_2 + 0.205H_3 I_a \left(\frac{\Delta x}{2}\right)$$

where ΔZ is the assumed thickness of the conductor, I_a is the current density, H is the VLF-EM data and ΔX is the interval between stations. The resulting profile data can then be analyzed and modeled using 2D inversion to analyze the conductivity sources of data.

Profile 2. Line 2 (Figure 11) has a baseline value of -5.4% with most of the SE section of the line being average. At the 100 and 160-meter marks, there are positive spikes in the IP and OP data to 138.2% and 66.4%, respectively. One negative spike is located around the 165-meter

mark, down to -77.2%. At the 225-meter mark, there is a spike in OP data up to 84%, but does not have a corresponding IP spike. Instead, there is a broad high in the IP data between 225 and 275-meter marks.

Profile 3. This line is situated just south of Line 2 (Figure 12). The IP and OP profiles generally mirror each other. At 40 meters, the IP data spikes to 313.5% and the OP data drops to -235%. At the 110-meter mark, they invert, with the IP data dropping to -235% and the OP data peaking at 221%. IP and OP data peaks at 200 and 250 meters are up to around 80%, and two more IP and OP maxima at 250 and 275 meters are at 40%.

Profile 4. Line 4 (Figure 13) has two IP and OP maxima at 50 and 75 meters, with a drop between them at 60 meters. Between 100 meters and 150 meters, there is a IP and OP minimum around 50%. The next IP and OP maximum is around 150 meters, up to 25%, then an IP and OP minimum at 250 meters down to -66%.

Profile 7. Line 7 (Figure 14) has a IP and OP maximum at the 48 meter, with the IP data up to 158% and OP data up to 76%. At 63 meters, both the IP and OP data are down to -87%, followed by a maximum IP and OP value between 70 meters and 80 meters at 76%. Next, the OP data drops to -87% at 105 meters, then peaks at 120 meters to 76%. The IP stays flatter, with a broad low at -45% between 80 meters and 110 meters. The final maximum is at 130 meters 75% for the IP and 25% for the OP data.

VLF-EM Fraser Pseudosection Analysis. Fraser depth pseudosections were created from the raw IP and OP VLF-EM data to image the near-surface vertical conductors near the Little Fanney Mine. The pseudosections show areas of high current density, as small eddy currents are formed in areas of higher conductivity. The depths of the sections range from 62

meters to 150 meters. These sections provide a semi-quantitative analysis of near-surface veins, fractures, and vertical conductors.

Profile 2. The IP component of line 2 has a high current density between 100 meters and 150 meters (Figure 15). The high-density area is sub-vertical, dipping slightly to the east. The highest current densities are found between the surface and around 60 meters. There is another small, less-dense zone at the 175-meter mark, but it only reaches 33 meters. This zone is also sub-vertical, dipping slightly to the west. The OP component shows a similar conductivity patterns as the IP image. There is an additional conductor around 225 meters, bounding a low conductivity region.

Profile 3. The IP component of line 3 has a high conductivity zone at 100 meters (Figure 15). It is much thinner, and shallower than line 2 (Figure 16), but also vertical. The OP component shows more conductivity maxima, with one centered at 100 meters, and one at 200 meters. Both bodies are vertical.

Profile 4. The IP component of line 4 shows a much higher current density zone between 50 meters and 100 meters (Figure 17). The model can be broken into two systems: an east-dipping high current density zone at 50 meters, and a west-dipping high-density zone at 80 meters. These two systems meet at a depth of 60 meters, where the dominant dip is east. At 250 meters, there is a low-density zone that dips sub-vertically to the west. The OP component shows similar conductive features between 50 and 100 meters, but has an additional wide, shallow conductor at 150 meters.

Profile 7. Line 7 shows one conductive zone at 50 meters on the IP component (Figure 18). This zone reaches a depth of 25 meters, and is dips to the east. The OP component shows an additional conductor at 80 meters dipping to the west, and one at 120 meters.

VLF-EM K-H Filter Analysis. The K-H filter is better at identifying smaller localized conductors, than the Fraser pseudosections (Karous and Hjelt, 1983). The Karous-Hjelt filter was produced by using the following equation in VLF2DMF from methods by Karous and Hjelt (1983):

$$\frac{\Delta Z}{2\pi Ia(0)} = 0.102H_{-3} + 0.059H_{-2} - 0.0561H_{-1} + 0.561H_1 - 0.059H_2 + 0.102H_3$$

Where $Ia(0) = 0.5[I\left(\frac{\Delta X}{2}\right) + I\left(-\frac{\Delta X}{2}\right)]$ and H_{-3}, H_{-2}, etc. are measured IP or OP data along the profile. ΔX is the interval between stations; ΔZ is the assumed thickness of the vertical conductor and$I$ is the induced current density. This filter provides a more detailed view of the subsurface conductivity structures than a Fraser filter (Karous and Hjelt, 1983). The maximum depth of the sections is less than the Fraser filter results, reaching a maximum depth of 70 meters. Generally, these two components display similar structures, but are the inverse of each other.

Profile 2. The K-H filtered real (IP) and imaginary (OP) components of this line show similar trends of high density currents between 100 and 175 meters, adjacent to low conductivity (Figure 19). The conductivity minima between 175 and 215 meters is sub-vertical, dipping east. The OP component of Line 2 has a similar chaotic nature to the conductive zone between 100 and 175 meters, but there has a more conductive thin area at 175 meters that is absent in the IP component. The area between 200 meters and 250 meters is more conductive, with a slight dip to the west. The OP component shows similar patterns of conductivity maxima as the IP sections, but there is an additional broad conductivity maxima between 200 and 250 meters.

Profile 3. The IP component of this profile shows a small area of conductivity at 100 meters, though it only reaches a depth of 10 meters (Figure 20). A low conductivity linear body

is situated at 125 meters, and reaches a depth of 45 meters. The rest of the IP component profile has no obvious conductive features. The OP component is the inverse of the IP component, and shows the deeper linear feature as having a high current density. In both cases, the deeper feature dips to the east. The OP component shows a conductivity maxima where the IP component has a conductivity minima.

Profile 4. The IP component of this profile has two thin high-current density zones between 50 meters and 75 meters (Figure 21). They are dipping toward each other, but only reaching a depth of 25 meters. At 125 meters, there is a deeper linear feature with less current density, starting at 25 meters and reaching 45 meters. Finally, another linear feature is found between 150 meters and 175 meters at a depth of 20 meters to 40 meters. Both features are dipping east. In the OP component, the feature between 50 meters and 75 meters still has higher current density, but not as high as in the IP component. The feature at 150 meters shows high current density. The OP component shows similar conductivity maxima as the IP component, however, the structure between 150 and 175 meters has a higher conductivity.

Profile 7. Finally, this profile shows high amplitude high-current density zones in both the IP and OP components (Figure 22). A thin linear feature is found at the 80-meter mark, reaching a depth of 21 meters. Another conductive zone is seen between 40 meters and 60 meters, but this is less defined, and shallower. There is a zone of low conductivity between 90 meters and 110 meters that is not well defined. The OP component shows similar conductivity maxima as the IP component, especially with the structure at 80 meters. The OP component also has a strong conductivity minima at 100 meters dipping to the west.

VLF-EM 2D Inversion. The VLF-EM IP and OP data were inverted for a 2D conductivity model using the following equation after Sasaki (1989):

$$[(J^T J + \lambda C^T C)]\delta p = J^T b$$

Where, δp represents the vector with the corrections applicable to parameters of the initial model, b is the vector of the differences between observed and calculated tipper components, J is the Jacobian matrix, T is the transpose operation, and λ is a Lagrange multiplier used to control the amplitude of the parameter corrections. Finally, C is the coefficient of values of roughness.

The final models (Figures 23-30) show regions of higher and lower resistivity. The following parameters were used for each model: Damping Factor: 3; Damping Decrease Factor: 0.9; Number of Iterations: 10; Data Error (RePart): 0.1; Data Error (ImPart): 0.1. Fractures and veins are likely to have lower resistivity due to the presence of groundwater, clays and/or conductive sulfides. Also included are the VLF-EM data (IP and OP) and model response (calculated data) for each profile (Figures 23, 25, 27, and 29).

Model 2. Model 2 has dominant conductivity bodies that lie horizontally near the surface (model response: Figure 23; model: Figure 24). There is a low conductivity body between 0 and 100 meters, then a higher conductivity body between 100 and 150 meters. Finally, there is another high conductivity body between 200 and 300 meters. These bodies are less than than 25 meters, and seem to follow the surface. Deeper bodies also seem to be parallel to the surface.

Model 3. This model also shows shallow conductivity maxima and minima (model response: Figure 25; model: Figure 26). First, a conductive body lies between 40 meters and 80 meters at a depth from 25 meters to 50 meters. This body lies below 20 meters of background conductivity. Next, a conductivity minima are located around the 100-meter mark at the surface to a depth of 50 meters. The next body is smaller, but more conductive at the 170 meters to 210

meters. It also lies at the surface to a depth of 25 meters. One smaller body lies at 270 meters and has a depth of 25 meters. Finally, a large linear conductive body lies between 300 and 450 meters with a depth of 50 meters.

Model 4. This model also has a combination of low and high conductive near-surface bodies (model response: Figure 27; model: Figure 28). The low conductive bodies are located between 0, 40 meters, 180, and 250 meters. Both bodies are shallow, reaching depths of 20 meters. The higher conductive bodies are located between 50 and 100 meters, 125 and 170 meters, and 275 and 325 meters. These bodies have a depth of 50 meters.

Model 7. Model 7 has one low conductive zone between 0 and 20 meters horizontal to the surface, and a depth of 25 meters (model response: Figure 29; model: Figure 30). Three high conductive zones are found between 30 and 50 meters, at 70 meters and finally between 110 and 170 meters. These bodies are also parallel to the surface, and reach depths of 25 meters.

Discussion

Queen Fault Analysis. The Queen Vein was the central focus of this study, but most of the VLF-EM analysis did not indicate the presence of a high conductivity values along the fault. The Queen Fault and vein, dips 70 degrees to the east, so any conductivity anomalies at depth should be east of the surficial expression. The magnetic map (Figure 6) shows no offset along the Queen Fault. The Queen fault offsets the Last Chance Andesite and Fanney Rhyolite, which probably have different magnetic susceptibility values, however there is no offset in the magnetic anomaly map. The east-west magnetic anomaly (Figure 6) seems to widen near the Queen Fault. This could be an indication of magnetic minerals at depth. However, the same region on the

Hilbert transformed VLF-EM map (Figure 9) does not correlate with the observed magnetic high.

K-H filtering and Fraser pseudosections along the northern section near the intersection of the Independence fault (Figures 15, 16, 19, and 20) indicate no obvious high conductivity regions, however, the 2D VLF-EM models (Figures 24 and 26) show a broad low resistivity? zone at the Queen vein. This high conductivity region could be from a change in composition from host rock to mineralized veins.

The above interpretations can be indicative of a mostly un-mineralized vein system, which matches observations made by Ferguson (1927) and Ratte (1981). There may be small isolated patches of conductive sulfides, but the system appears to be discontinuous.

Graveyard Fault Analysis. In general, all the VLF filtering methods agree with each other in terms of the location of conductivity anomalies (Figures 11-30). The magnetic anomaly map (Figure 6) indicates a magnetic maxima between the Graveyard fault and the Queen fault that trends east-west. The trend of the anomaly does not follow any of the known faults in the region. The Graveyard fault does separate a magnetic minima from a higher magnetic anomaly. This is likely caused by the Graveyard fault offsetting different sections of the Last Chance andesite. A magnetic maxima near the intersection of the Queen fault and Graveyard fault. Ferguson (1927) and Ratte (1981) identified this unit as the Last Chance Andesite; however, the magnetic anomaly pattern is like that of Fanney rhyolite or the Deadwood member of the Fanney rhyolite. The Fanney rhyolite (seen north of the Independence fault) has a higher magnetic susceptibility content than the Mineral Creek andesite and the Last Chance andesite. The Independence Fault is proposed to crosscut the Graveyard fault where Ferguson (1927) marked

the transition from mineralized to un-mineralized. There is no magnetic anomaly offset along the northern portion of the Graveyard fault as it connects with the Queen fault.

The Hilbert Transform VLF-EM anomaly map indicates similar anomaly patterns as seen on the magnetic anomaly map (Figure 9). A high amplitude linear conductivity body crosscuts the Graveyard fault in the same area. There is not an obvious difference between the conductivity anomalies east and west of the Graveyard Fault. The Independence fault crosscut relationship noted above is also seen just north of the mineralized un-mineralized transition along the Graveyard fault (Figure 9). This suggests that the Graveyard Fault is relatively barren of conductive minerals. The K-H pseudosections (Figures 21 and 22) show thinner bodies in this region, while the Fraser pseudosections (Figures 17 and 18) show wider bodies. Line 4 (Figure 17) has a high amplitude conductivity body on the NW end of the line. The K-H pseudosection (Figure 21) shows two thin conductivity bodies dipping sub-vertically toward each other, while the Fraser pseudosection (Figure 17) shows larger conductivity bodies that merge at depth. This zone is located just west of the west-dipping Graveyard Fault. Due to the west-dipping nature of the Graveyard fault, we would expect any mineralization at depth to be west of the Graveyard fault.

Lines 2 and 3 (Figures 15 and 16) show no conductivity anomalies near the Graveyard fault suggesting that any mineralization that may have been present near Line 4 is either absent or is at a greater depth. This would suggest that mineralization along the Graveyard vein is highly discontinuous.

Independence Vein Analysis. Though the Independence fault was not the original focus of this study, it has the most mineralogical potential based on our geophysical analysis. The Independence Fault was mapped by Ferguson (1927) and Ratte (1981) as barren from the

intersection with the Queen fault to the intersection of the Ida May fault to the west. They also mapped the Independence Fault truncating into the Queen fault. Further analysis of the magnetic anomaly map show a large gradient across the Independence Fault (Figure 6). This gradient continues past the Queen Fault and through the Graveyard Fault. This anomaly pattern implies that the Independence Fault continues east, rather than truncating into the Queen Fault. This is also supported by the Hilbert transformed VLF-EM map (Figure 9). This map shows a series of conductivity maxima along the steep magnetic gradient east of the Queen Fault (Figure 9). The area between the Queen Fault and the Graveyard Fault is covered by overburden, obscuring the surface geology.

Conductivity maxima in both the K-H and Fraser pseudosections are present along the Independence vein. These regions align where the lines crossed the Independence Fault, near the intersection of the Queen Fault. Furthermore, the 2D models (Figures 24 and 26) also show conductivity maxima in the location of the Independence fault. Both observations clearly show that a conductive body may be present at depth, or concealed by overburden.

Summary of Discussion. The results of the VLF-EM filtering, inversion and anomaly map along with the magnetic anomaly map indicated possible new structures and mineralization areas within the Consolidated Mine project area. The analysis shows that the Queen Fault is barren of conductive and magnetic minerals. Small pockets of conductive minerals may be present near the junction of the Fanney fault, but previous companies mainly mined these out. Additionally, the Graveyard Fault shows little expression of conductive minerals, but does show some offset between higher magnetic and lower magnetic anomalies of the Last Chance Andesite. Finally, the Independence Fault is associated with high amplitude conductivity anomalies near the junction with the Queen Fault, though no surface expression of mineralization

is present. Furthermore, the Independence Fault seems to continue east, past the Queen Fault, and across the Graveyard fault, as evidenced by the VLF-EM Hilbert transformed and magnetic anomaly maps (Figures 6 and 9). This vein seems to hold the most promise as far as future exploration.

Temporal Summary of Mineralization. The geologic history of the Mogollon Mining District is very complex due to changing volcano-tectonic systems. Based on the geophysical analyses, the timing of extension and mineralization is more evident. Ferguson (1927) first noted that mineralization occurred after the eruption of the volcanic units in the district. Ratte (1981) further postulated that mineralization occurred after 15 Ma based on K-Ar ages of an andesite unit overlying the Dog Gulch Formation (older than the mineralization) north of the district. Finally, Houser (1987) concluded that mineralization occurred around the same time as the Basin and Range stage of the Alma Basin formation (~18 Ma).

A previous extensional event (23 Ma – 19 Ma) most likely activated the Queen fault and juxtaposed the Fanny Rhyolite – Mineral Creek Andesite stratigraphy next to the Deadwood member of the Fanney Rhyolite – Last Chance Andesite stratigraphy (up to 330 meters of displacement). This initial episode exploited the weakness of the Bursum caldera margin. This initial extensional event followed by a second event between 18 Ma and 15 Ma, and likely accommodated space for mineralization in the Mogollon Mining District. The temporal framework of this event is supported by a K-Ar age on adularia from a vein north of the Mogollon Mining District (Houser, 1994) and because mineralization is not crosscut by younger faults, implying active movement of the N-S and NW-SE faults as mineralization occurred. Furthermore, Ferguson (1927) and Bornhorst et al. (1984) noted that there is little evidence of boil-textures within the veins. This implies that mineralization was controlled by pressure

releases from incremental extension, therefore mineralization occurred as the Alma Basin was forming between 18 Ma and 15 Ma. This is further supported by our geophysical observations along the Independence fault. The NW-SE trending Independence fault appears to crosscut the Queen fault, which implies that both faults were active to accommodate oblique movement to the southwest.

In summary, the Bearwallow Mountain Andesite erupted and covered the Mogollon Mining District ~24 Ma, which was followed by initial extension to the west with oblique movement to the south between 23 Ma and 19 Ma (Houser, 1994). This oblique movement was accommodated in the mining district by reactivated caldera rim structures. To the south, most of the movement was perpendicular to the caldera structural margin, so none of the minor perpendicular caldera structures were reactivated (Ratte et al., 2006). Around 330 meters of vertical movement occurred along the Queen fault in the mining district (Ferguson, 1927; Ratte, 1981). Then, between 18 Ma and 15 Ma, further extension occurred, along with hydrothermal alteration and mineralization within the active faults. Both the N-S and NW-SE faults were active, and mineralization was continuous between the two. Little displacement occurred within the mining district during this event, with most accommodation most likely occurring in the Alma Basin. Finally, later extension occurred in the Alma Basin, leaving the mining district unaffected by major displacement. Some slicken lines can be found between different veins, indicating some post-mineralization movement.

Conclusions

After analysis of filtered VLF-EM data, inversion results, Hilbert transform results, and old maps of the district, we conclude the following:

1. The Independence Fault continues west, separating a small body of Deadwood member of Fanney Rhyolite to the north and last Chance Andesite to the South. This also provides evidence for little offset during mineralization.
2. Conductivity is high along the Independence vein, but there is no surface expression of veins, indicating possible buried conductive minerals.
3. The Queen fault does show surface expressions of veining, but does not have strong conductivity, indicating barren veins.
4. The Graveyard Fault shows no indication of conductive veins or offset of different magnetic bodies.
5. Most displacement in the district occurred prior to mineralization.

We propose that future exploration focus on the Independence fault because the results indicate a conductive body at depth, previous discoveries in the district came from unassuming surficial geology, and most economic mineralization is west of the Queen Vein. The VLF-EM system is a cheap and easy method to identify future drilling targets. However, these results should be taken with caution, as they are just models. Additional drilling and surficial mapping can further improve our models.

References

Anderson, J. B., 1939, A history of the Mogollon Mining District, New Mexico [Master's of Arts]: University of New Mexico, 136 p.

Bornhorst, T., and Kent, K. R., 1985, Geochemistry of host-rock alteration at the Eberle Mine, Mogollon Mining District, Southwestern New Mexico: New Mexico Bureau of Mines & Mineral Resources, p. 7-15.

Bornhorst, T. J., Kent, G. R., Mann, K. L., and Richey, S. R., 1984, Temperature of Mineralization in Mogollon Mining District and Vicinity, Southwest New Mexico: New Mexico Geology, p. 53-55.

Eveleth, R. W., 1979, New methods of working an old mine- case history of the Eberle Group, Mogollon, NM: New Mexico Geology, v. 1, p. 7-10.

Ferguson, H. G., 1927, Geology and Ore Deposits of the Mogollon Mining District, New Mexico: USGS Bulletin 787.

Fraser, D. C., 1969, Contouring of VLF-EM data: Geophysics, v. 34, no. 6, p. 958-967.

Hiner, J. E., 2016, 43-101 Technical Report on the Mogollon Project, Catron County, New Mexico, USA One World Investments Inc.

Houser, B. B., 1994, Geology of the late Cenozoic Alma Basin, New Mexico and Arizona: New Mexico Geological Society Guidebook, v. 45, p. 121-124.

Karous, M. and Hjelt, S., 1983, Linear filtering of VLF dip angle measurements, Geophysical Prospecting, v. 31. P. 782 - 794.

McIntosh, W. C., Chapin, C. E., Ratte, J. C., and Sutter, J. F., 1992, Time-stratigraphic framework for the Eocene-Oligocene Mogollon-Datil Volcanic Field, Southwest New Mexico: Geological Society of America Bulletin, v. 104.

O'Brien, D. P., 1971, CompDepth, a new method for depth to basement computation [abstract]: Geophysics, 38,187.

Ratte, J. C., 1975, Geologic setting and revised volcanic stratigraphy of the Mogollon Mining District, Catron County, New Mexico: USGS Open File Report 75-497.

Ratte, J. C., 1981, Geologic map of the Mogollon quadrangle, Catron County, New Mexico, 1557.

Ratté, J. C., Marvin, R. F., Naeser, C. W., and Bikerman, M., 1984, Calderas and ash flow tuffs of the Mogollon Mountains, Southwestern New Mexico: Journal of Geophysical Research, v. 89, p. 8713-8732.

Senterfit, R. M., Ratte, J. C., Kamilli, R. J., and Klein, D. P., 1996, Audiomagnetotelluric study of the Bursum Caldera and the Mogollon mining District, Southwest New Mexico: U.S. Geological Survey.

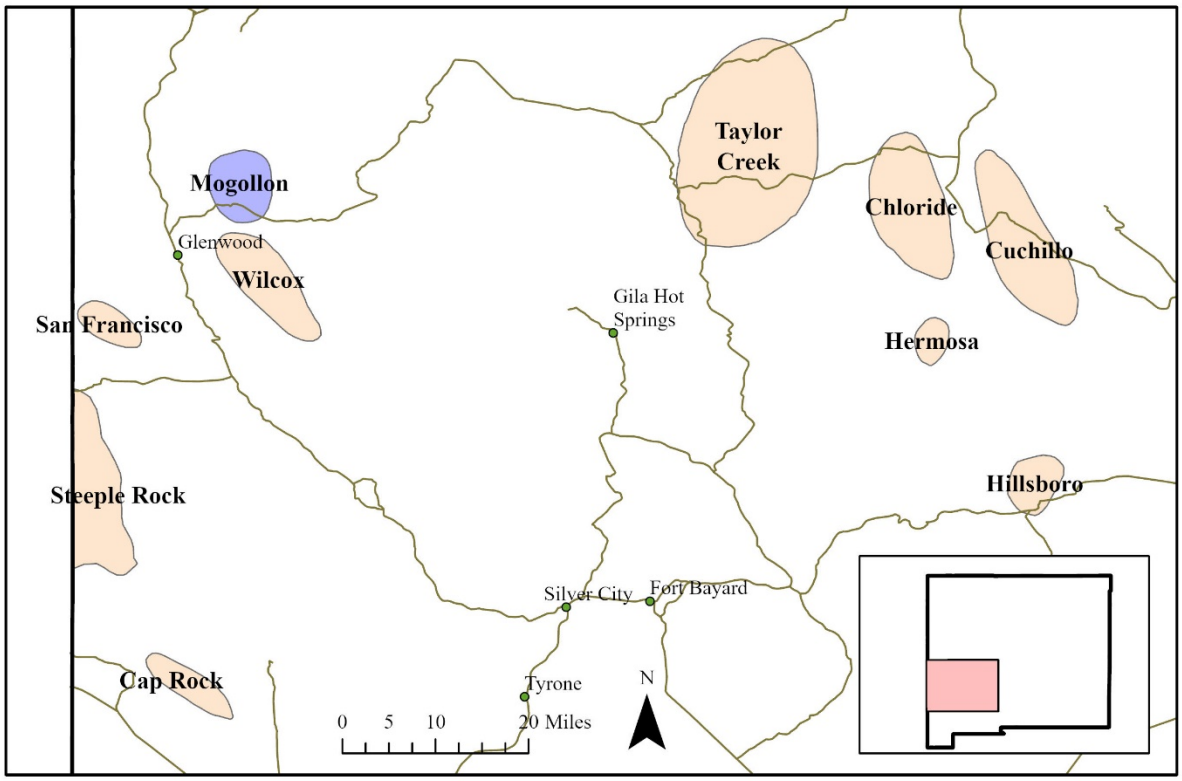

Figure 1: Map of precious metal mining districts in southwestern New Mexico, highlighting the Mogollon Mining District (purple).

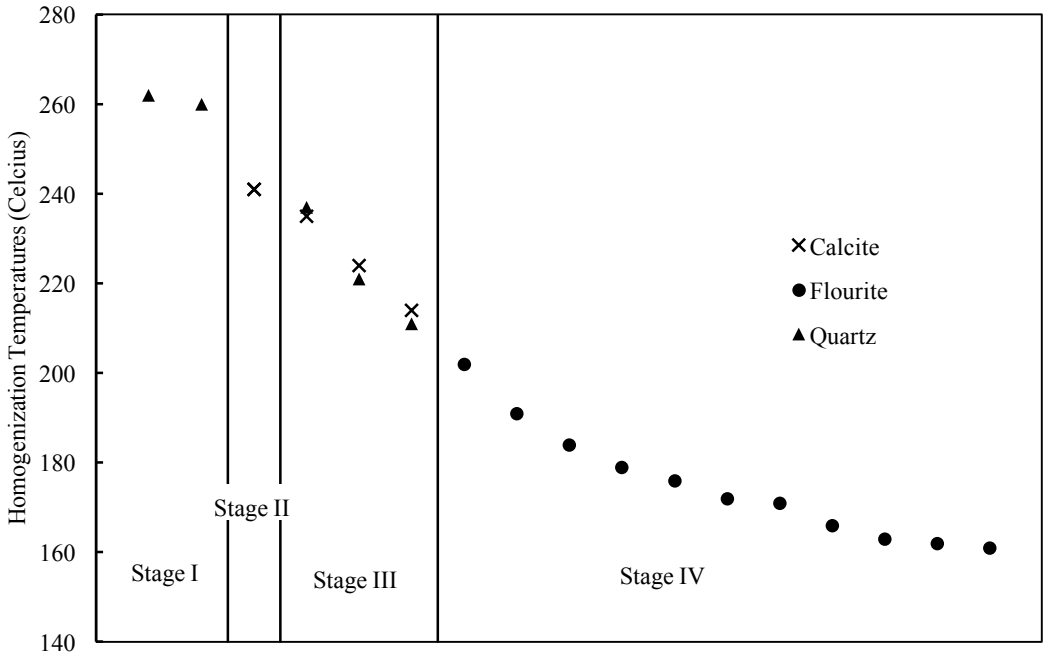

Figure 2: Plot of homogenization temperatures and different precipitation stages, after Bornhorst (1984). Stage I is a high temperature quartz precipitation, Stage II is a high temperature calcite phase, Stage III is a bimodal quartz and calcite phase, and Stage IV is a lower temperature fluorite phase.

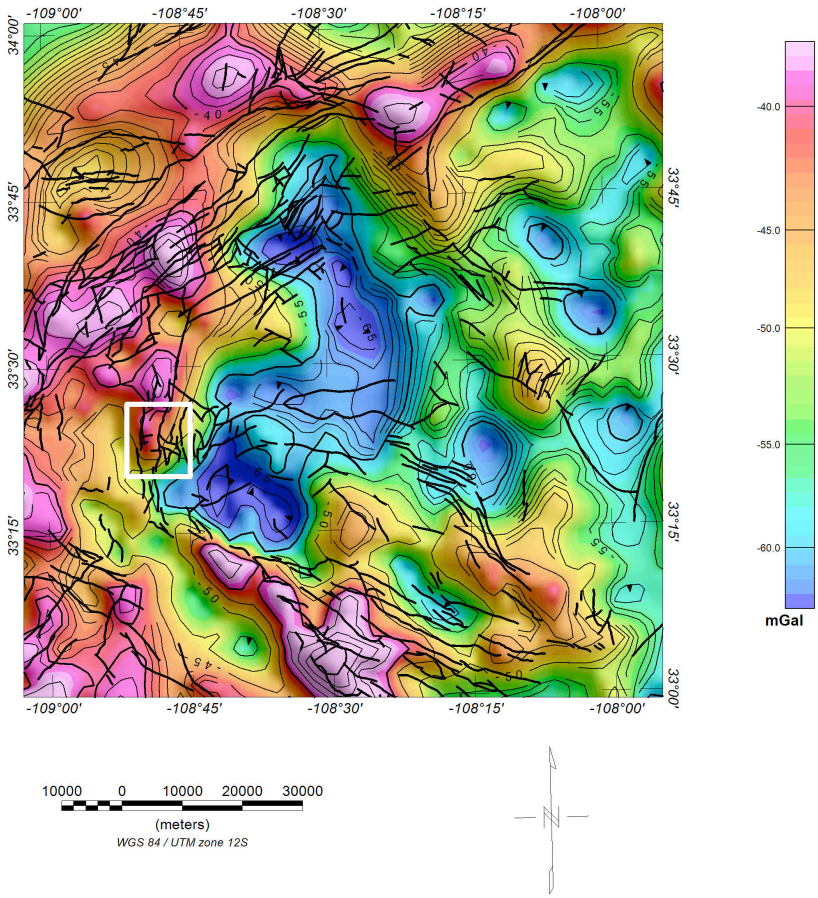

Figure 3: Isostatic residual gravity anomaly map of the Mogollon Mining District and the vicinity. Black lines are regional faults. The white box indicates the mining district location.

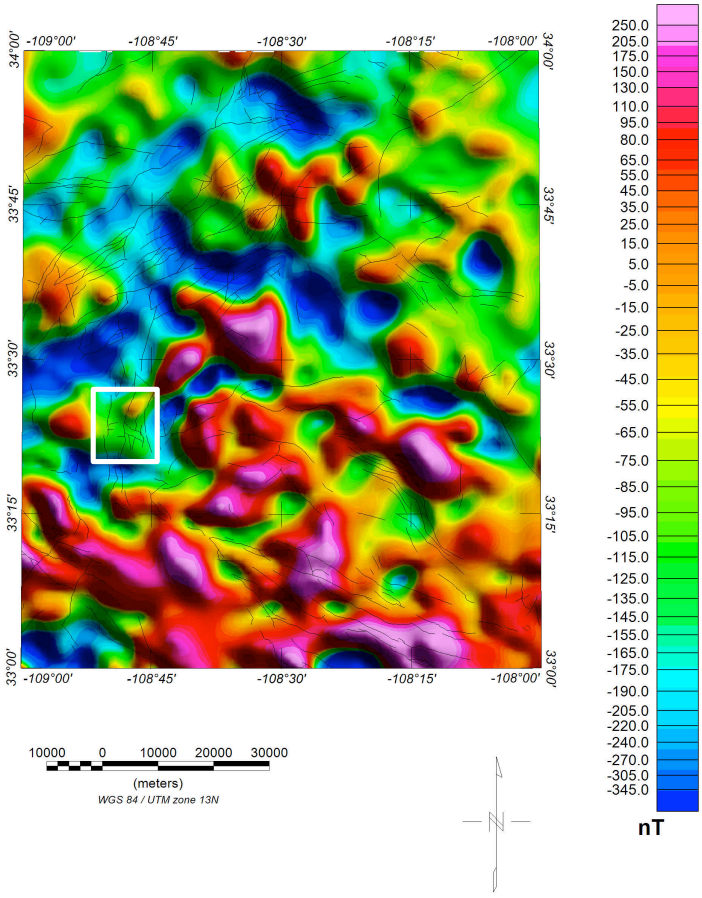

Figure 4: Total-field magnetic anomaly map of the Mogollon Mining District and vicinity. Black lines are the location of the volcanic units and regional faults. White box indicates the general location of the mining district.

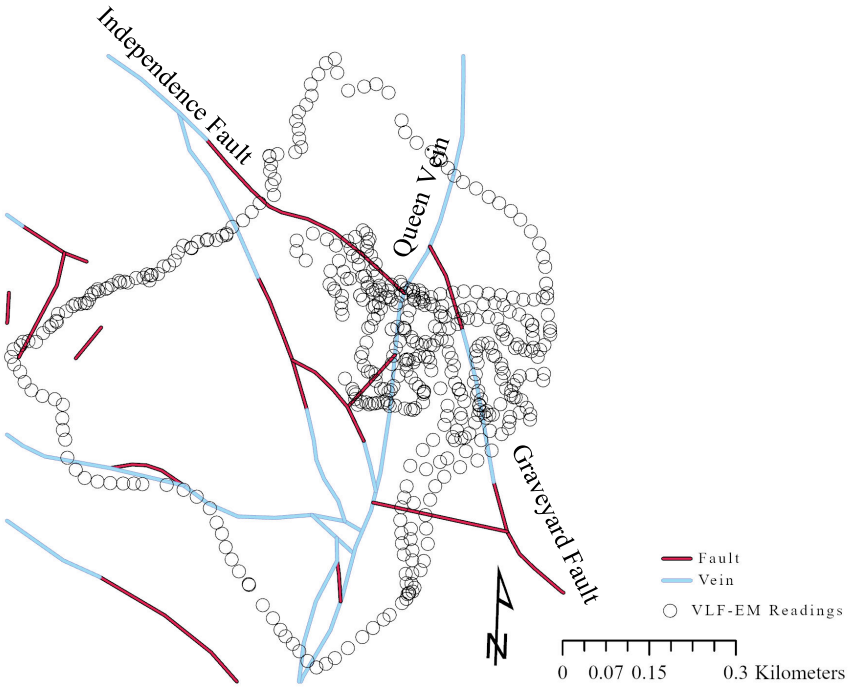

Figure 5: Location of VLF-EM station readings with unmineralized faults (red) and mineralized faults (blue).

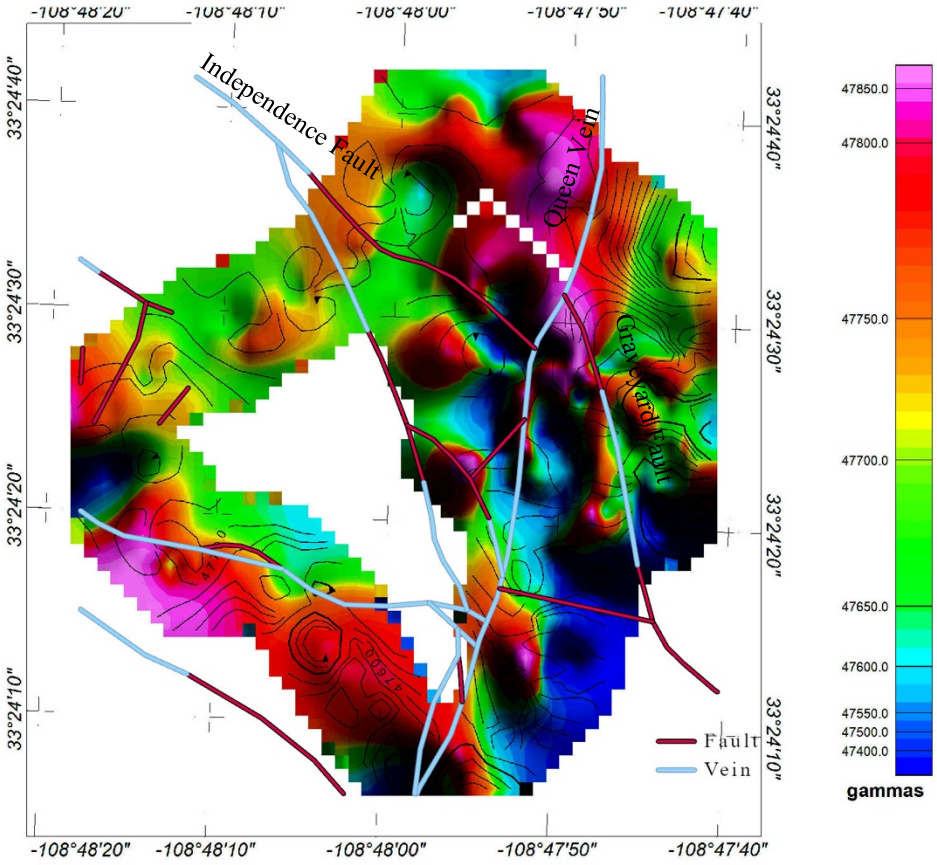

Figure 6: Magnetic data collected at the time of VLF-EM collection of the study area. Pink areas have a higher magnetic anomaly while blue areas have lower magnetic anomalies.

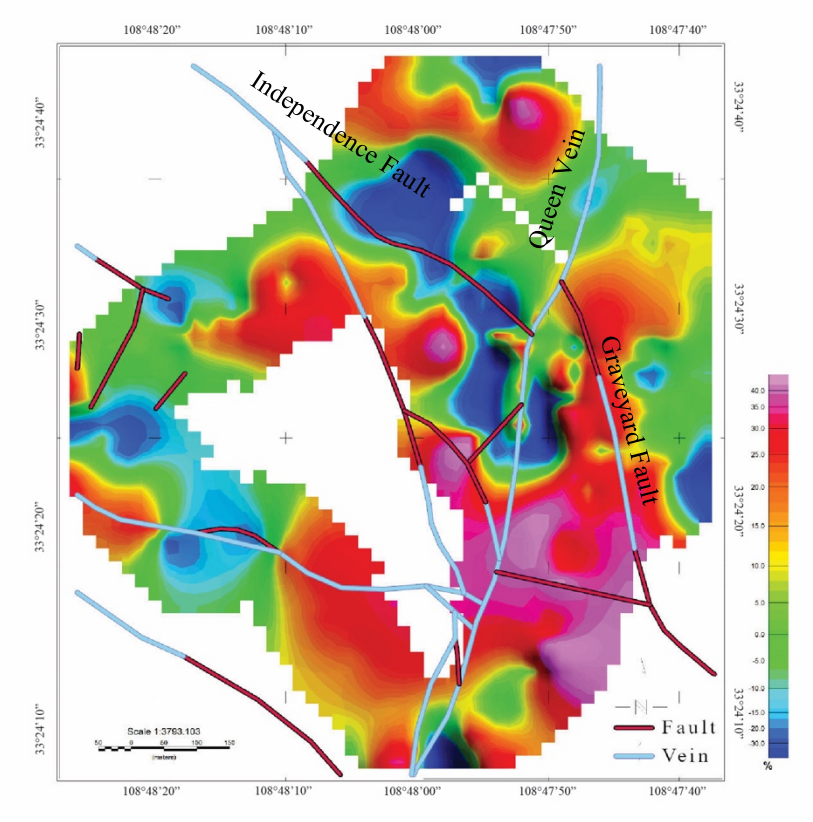

Figure 7: IP VLF-EM anomaly map of the study area with un-mineralized faults (red) and mineralized faults (blue).

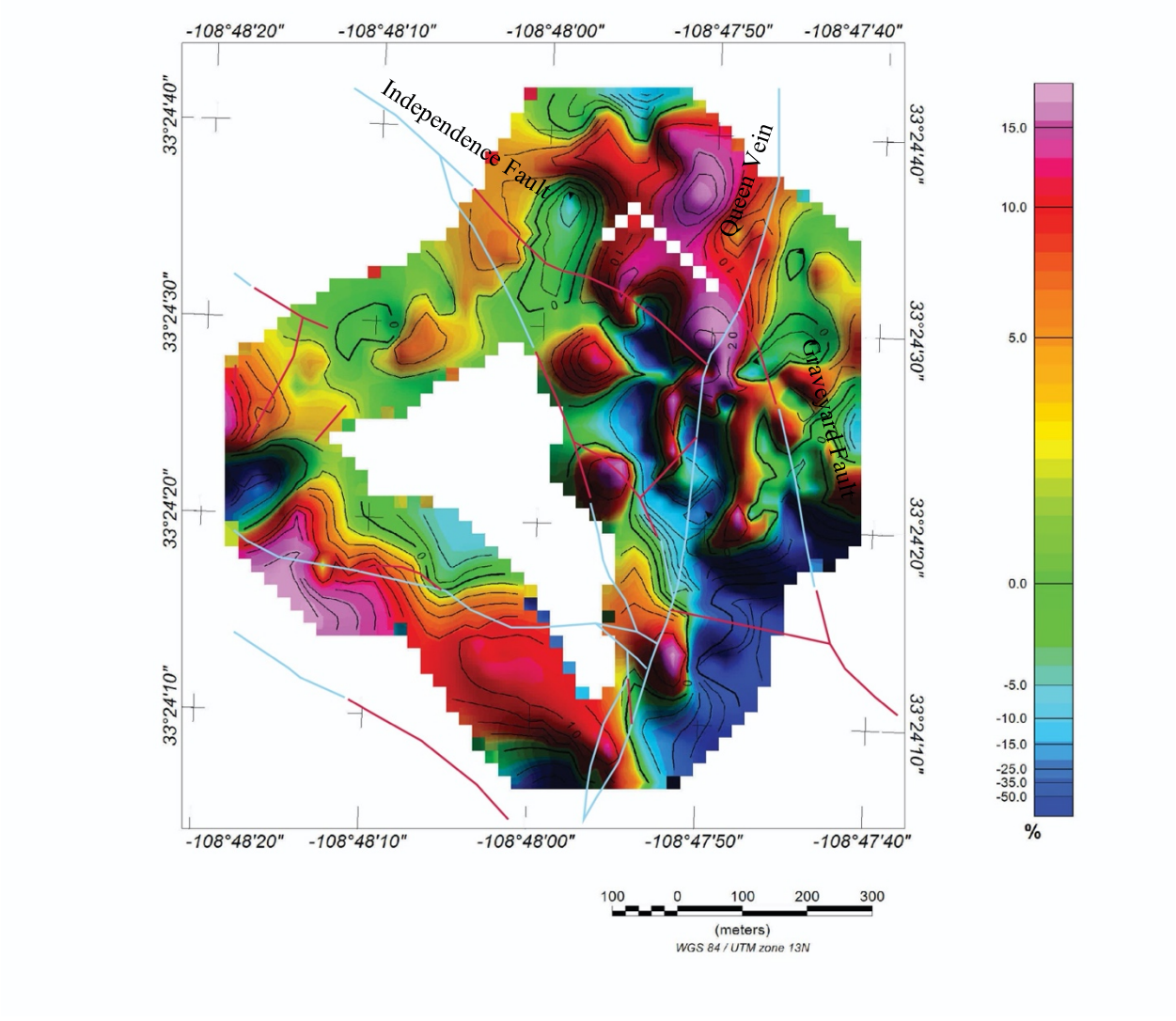

Figure 8: OP VLF-EM anomaly map of the study area.

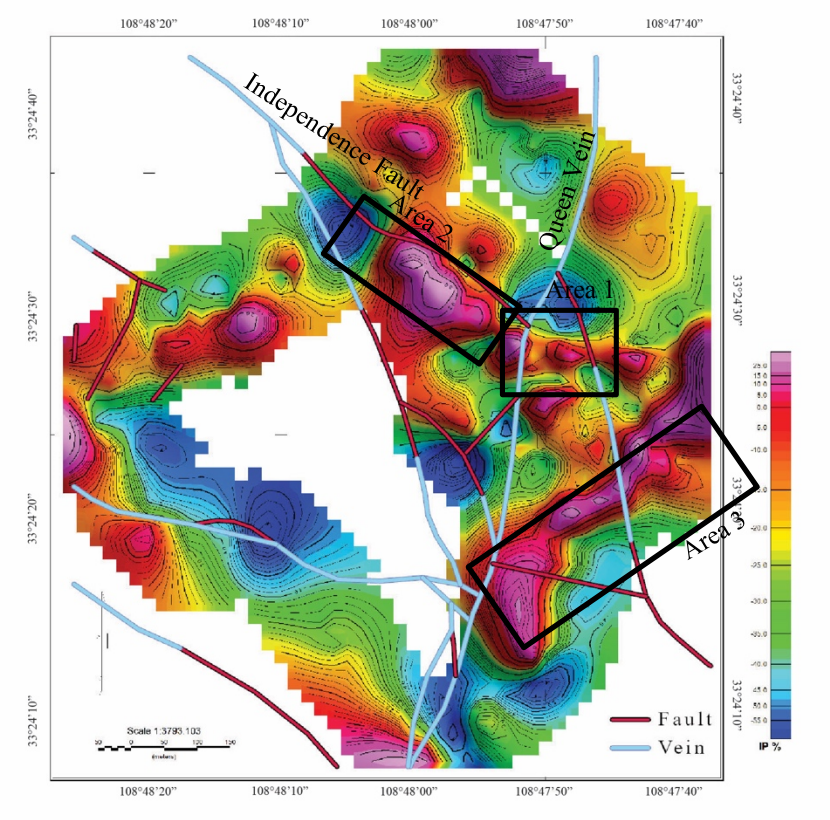

Figure 9: Hilbert transformed VLF-EM anomaly map of the study area. Faults are overlain showing mineralized (blue) and un-mineralized (red) zones. Black lines represent low resistivity zones.

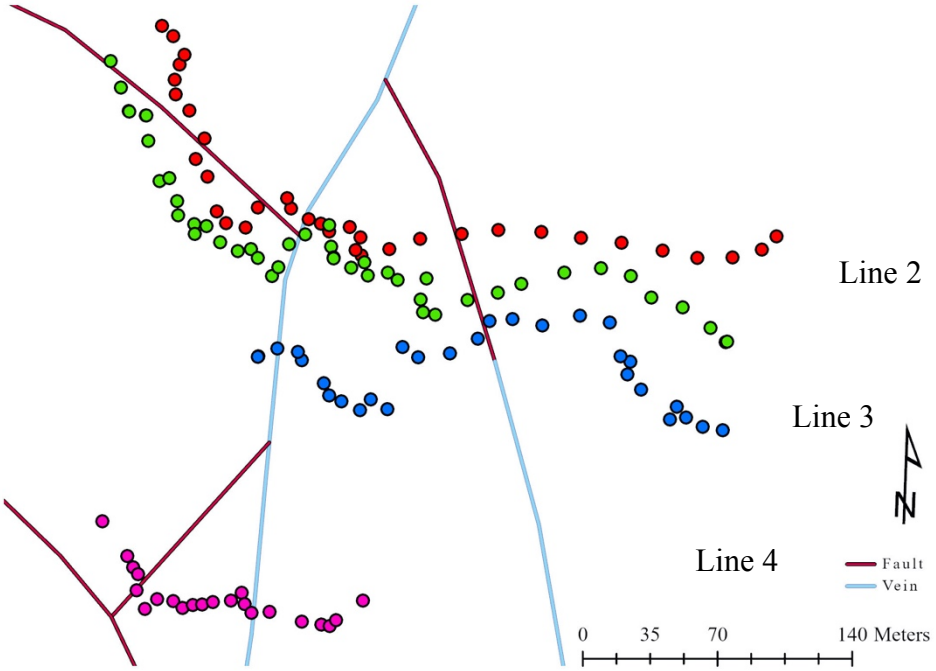

Figure 10: Locations of VLF-EM profiles modeled. Red dots show Line 2, green dots show Line 3, blue dots show Line 4, and pink dots show Line 7. Mineralized faults are blue lines and un-mineralized faults are red lines.

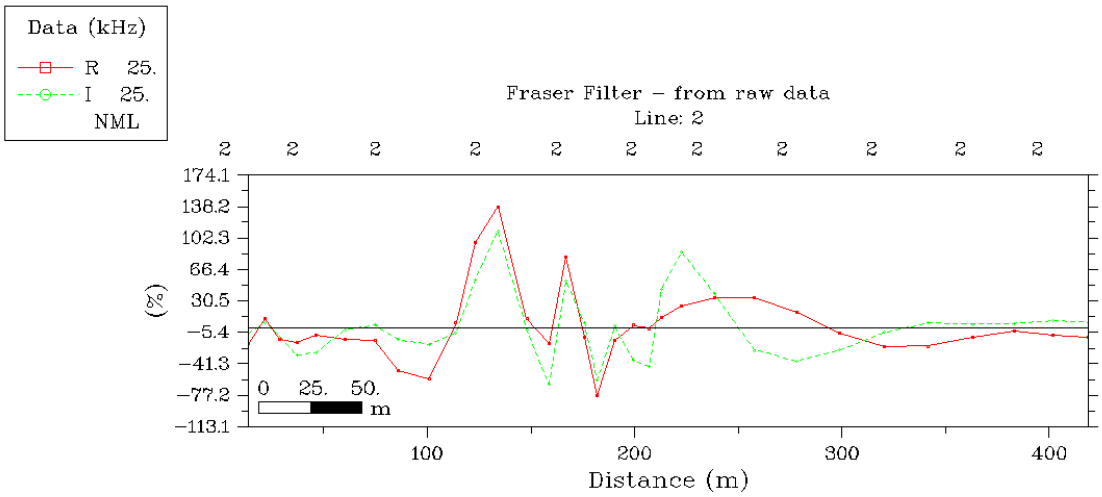

Figure 11: Fraser Filtered VLF-EM profile along line 2 in Figure 10. The red line is the real component (IP) while the green line is the imaginary component (OP).

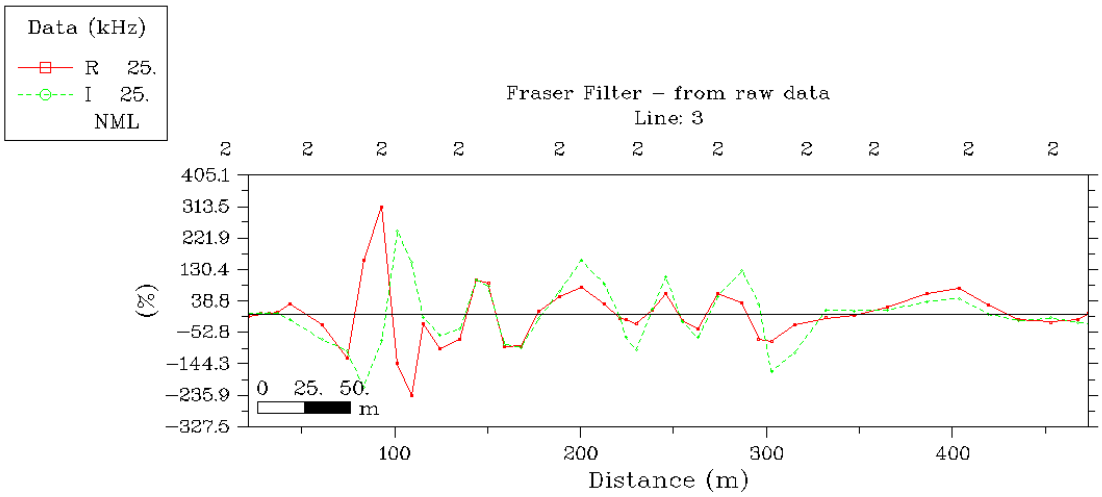

Figure 12: Fraser Filtered VLF-EM profile along line 3 in Figure 10. The red line is the real component while the green line is the imaginary component.

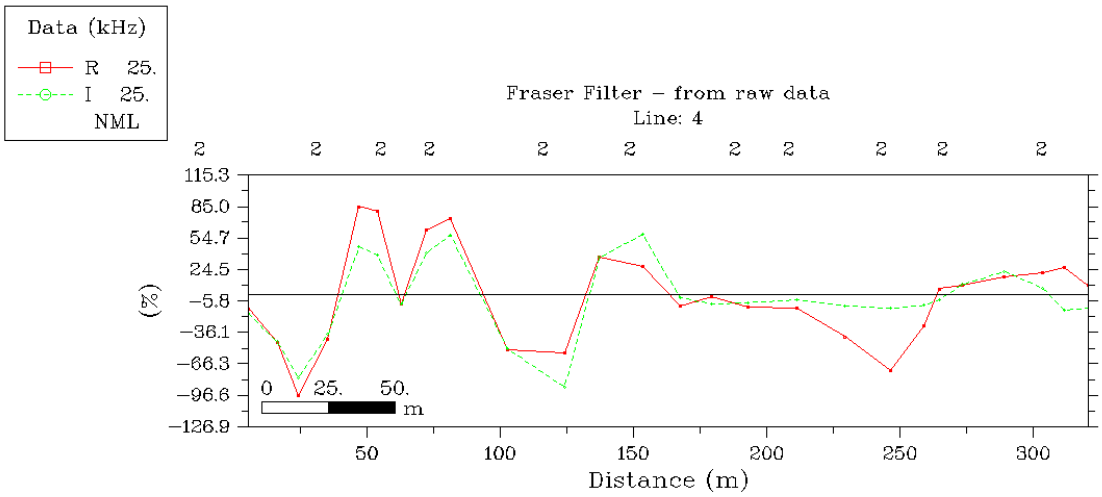

Figure 13: Fraser Filtered VLF-EM profile along line 4 in Figure 10. The red line is the real component while the green line is the imaginary component.

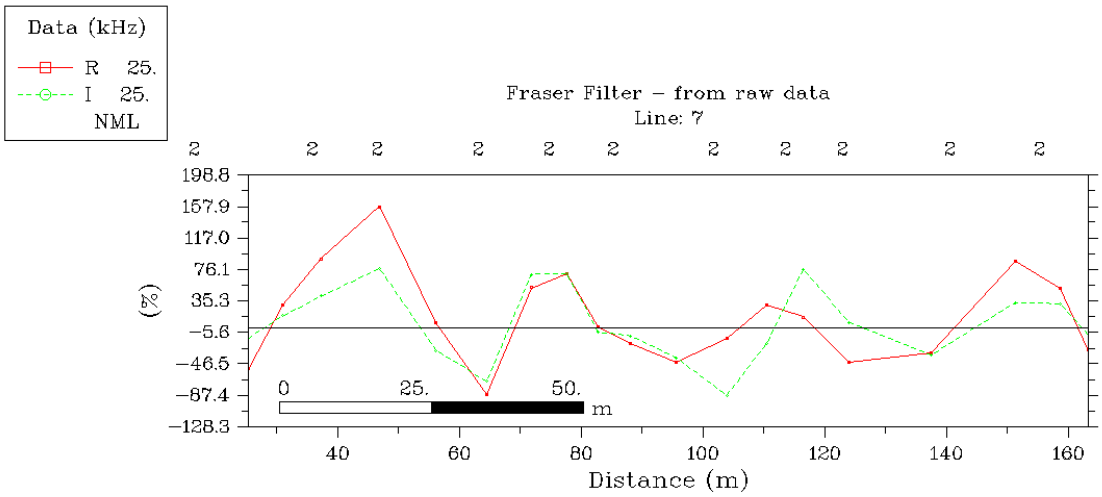

Figure 14: Fraser Filtered VLF-EM profile along line 7 in Figure 10. The red line is the real component while the green line is the imaginary component.

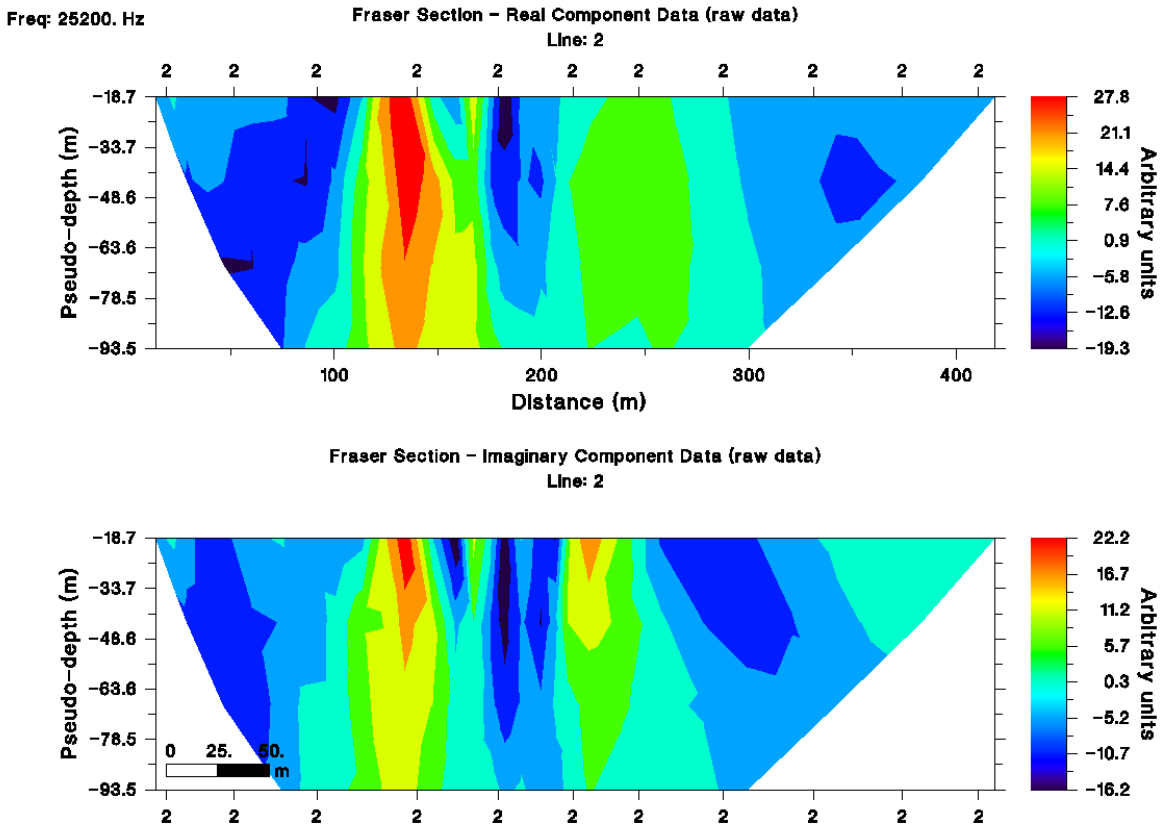

Figure 15: Fraser pseudosections derived from the VLF-EM data along profile 2 in Figure 10. Top figure is derived from the real component (IP) and the lower figure is derived from the imaginary component (OP).

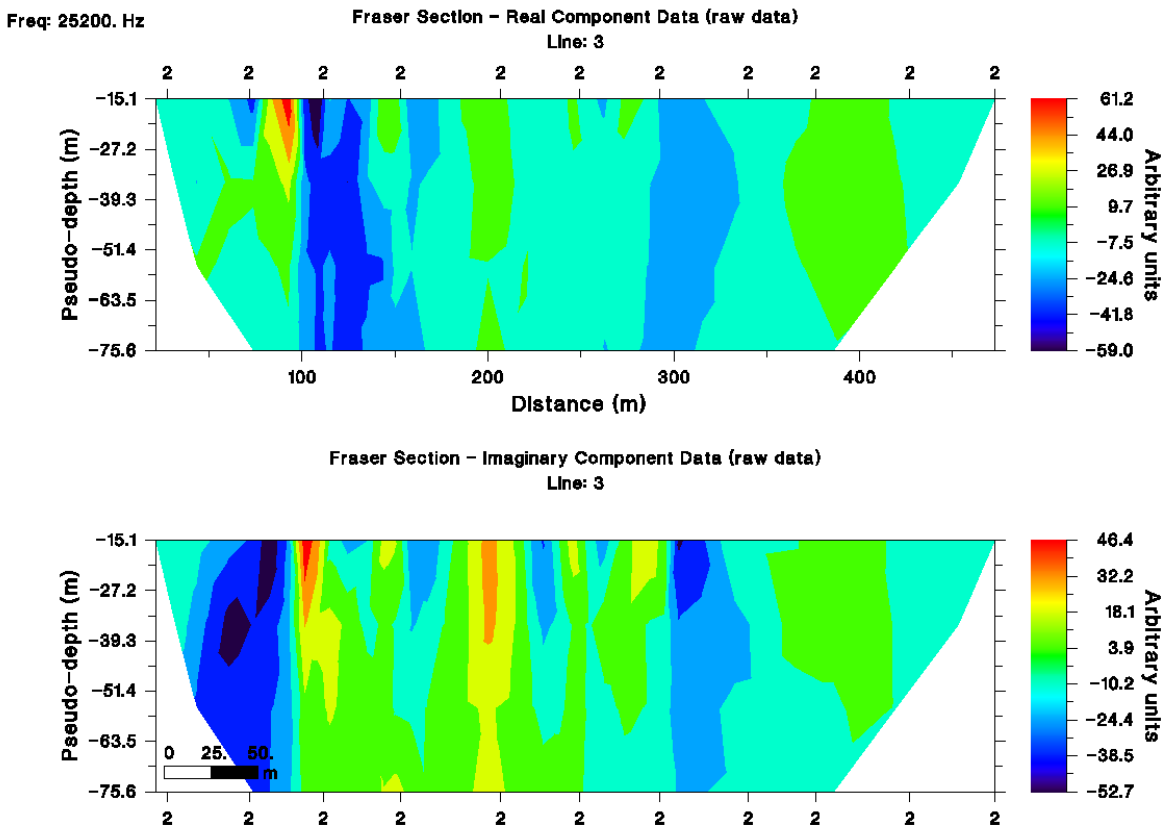

Figure 16: Fraser pseudosections modeled from VLF-EM data along profile 3 in Figure 10. Top figure is modeled from the real component and the lower figure is modeled from the imaginary component. Red areas indicate higher conductivity anomalies while blue areas indicate lower conductivity anomalies.

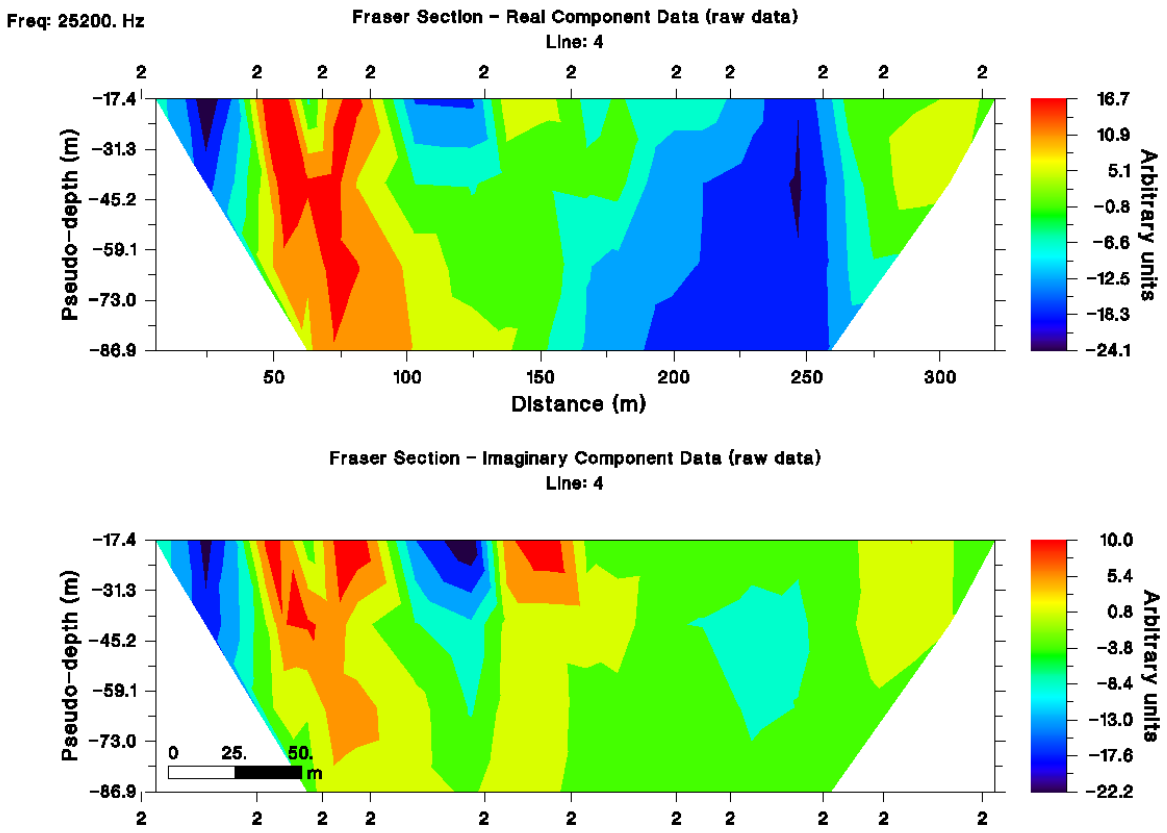

Figure 17: Fraser pseudosections modeled from VLF-EM data along profile 4 in Figure 10. Top figure is modeled from the real component and the lower figure is modeled from the imaginary component. Red areas indicate higher conductivity anomalies while blue areas indicate lower conductivity anomalies.

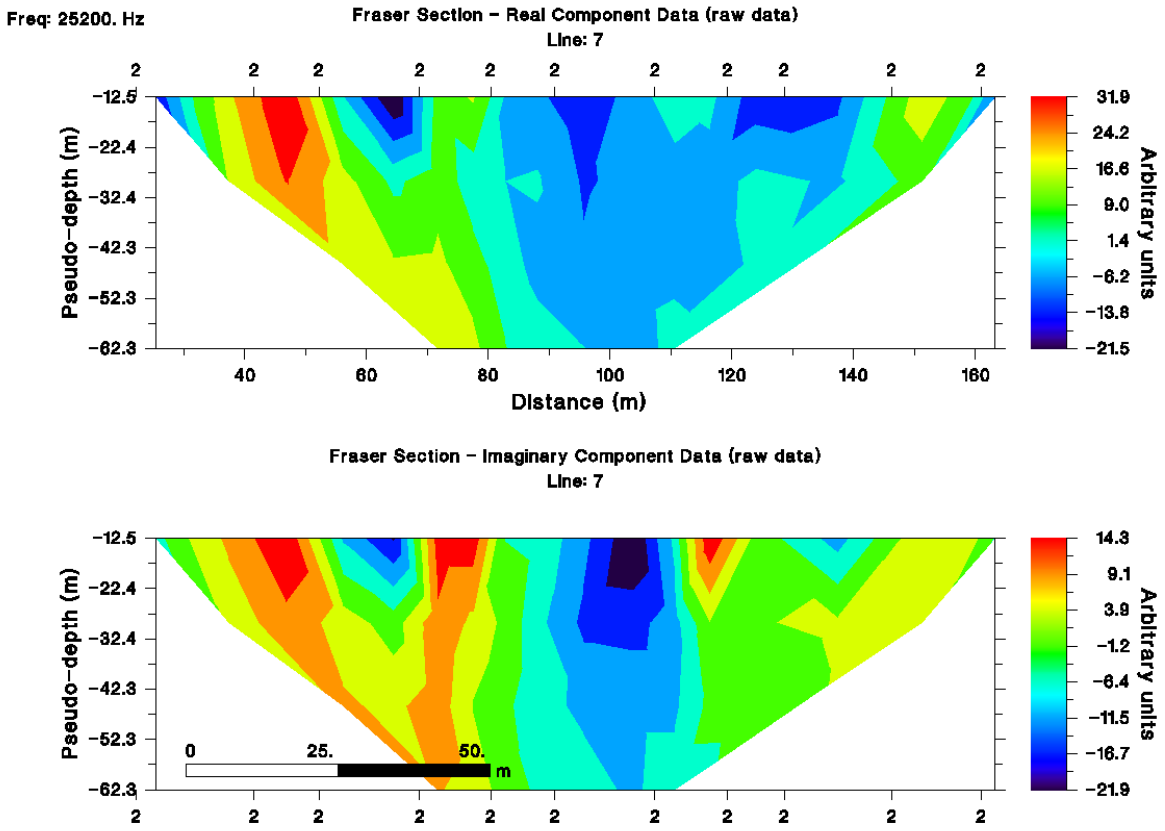

Figure 18: Fraser pseudosections modeled from VLF-EM data along profile 7 in Figure 10. Top figure is modeled from the real component and the lower figure is modeled from the imaginary component. Red areas indicate higher conductivity anomalies while blue areas indicate lower conductivity anomalies.

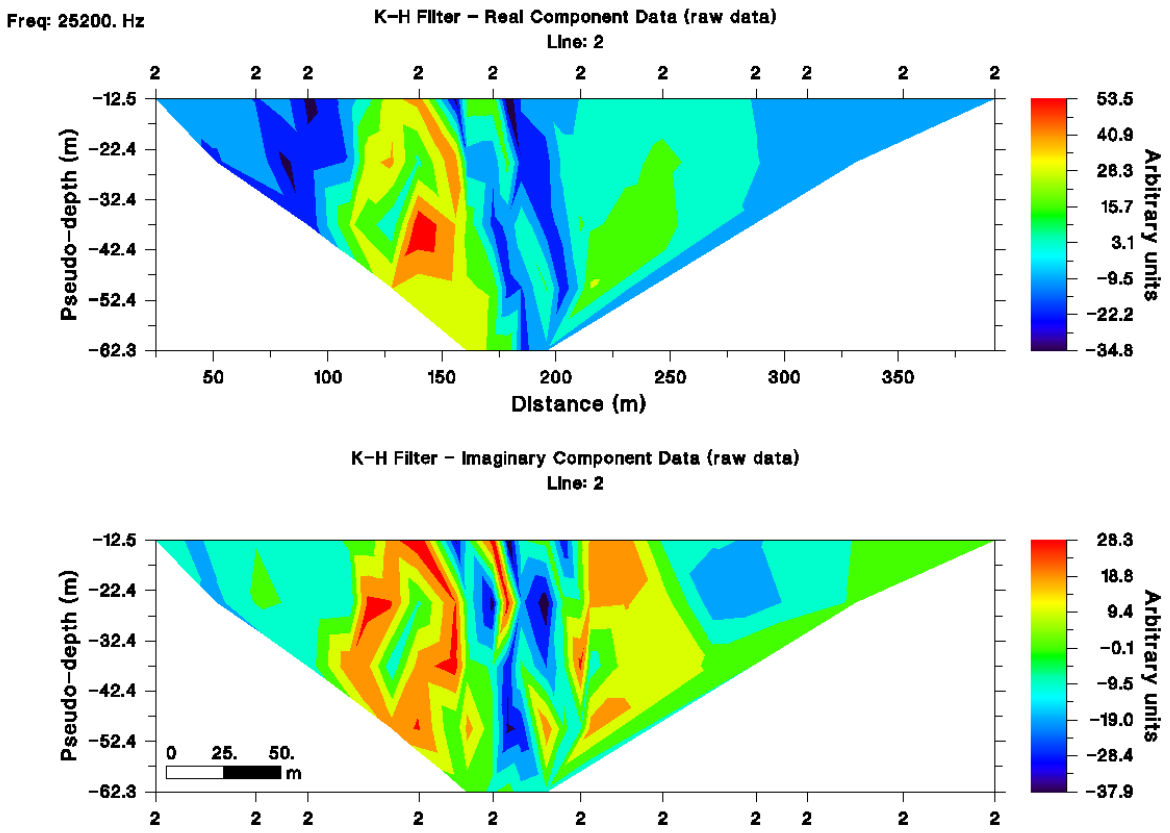

Figure 19: K-H filtered pseudosections derived from VLF-EM data along profile 2 in Figure 10. Top figure is derived from the real component (IP) and the lower figure is derived from the imaginary component (OP). Do for all KH profiles

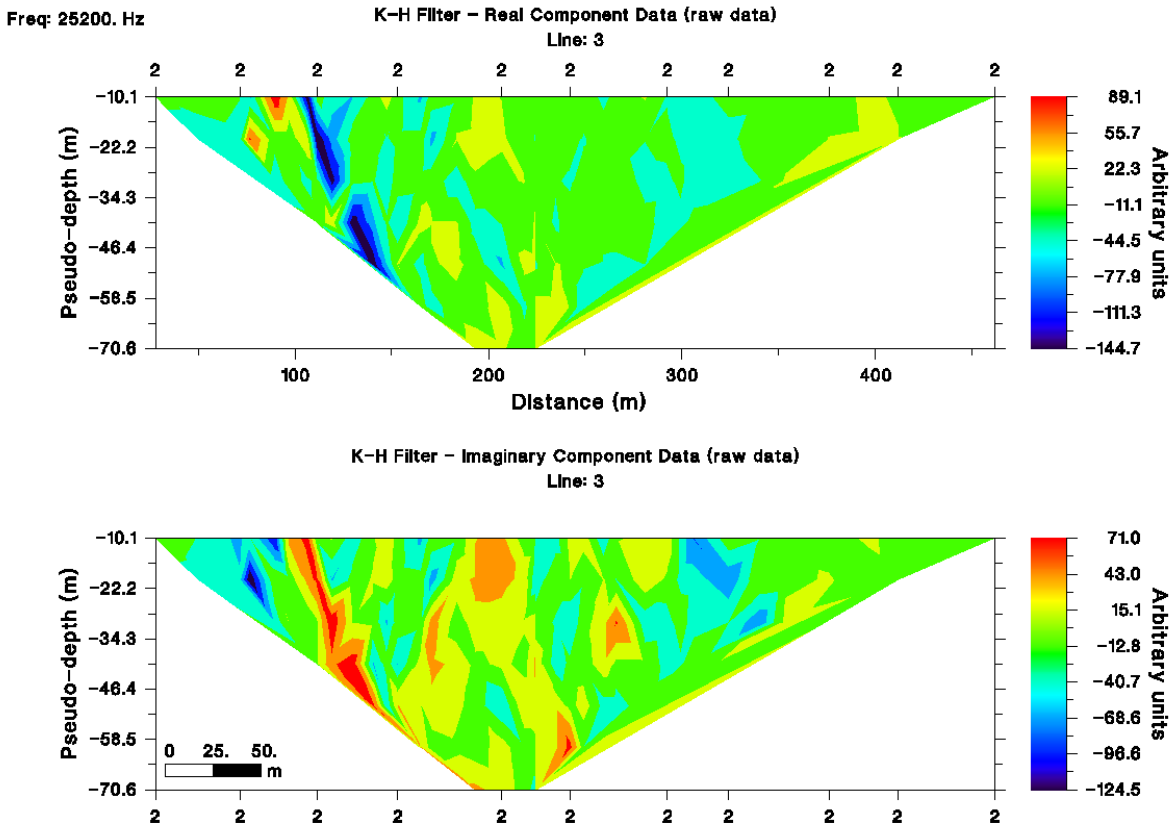

Figure 20: K-H filtered pseudosections modeled from VLF-EM data along profile 3 in Figure 10. Top figure is modeled from the real component and the lower figure is modeled from the imaginary component. Red areas indicate higher conductivity anomalies while blue areas indicate lower conductivity anomalies.

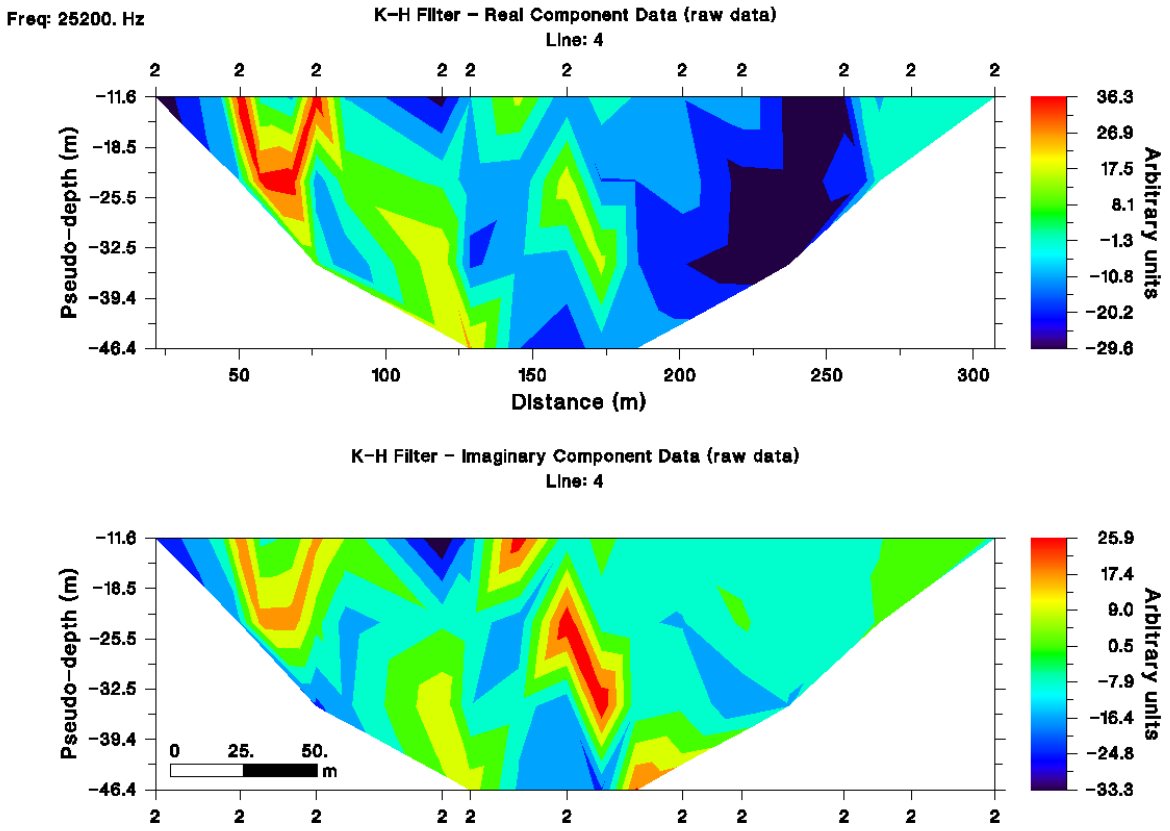

Figure 21: K-H filtered pseudosections modeled from VLF-EM data along profile 4 in Figure 10. Top figure is modeled from the real component and the lower figure is modeled from the imaginary component. Red areas indicate higher conductivity anomalies while blue areas indicate lower conductivity anomalies.

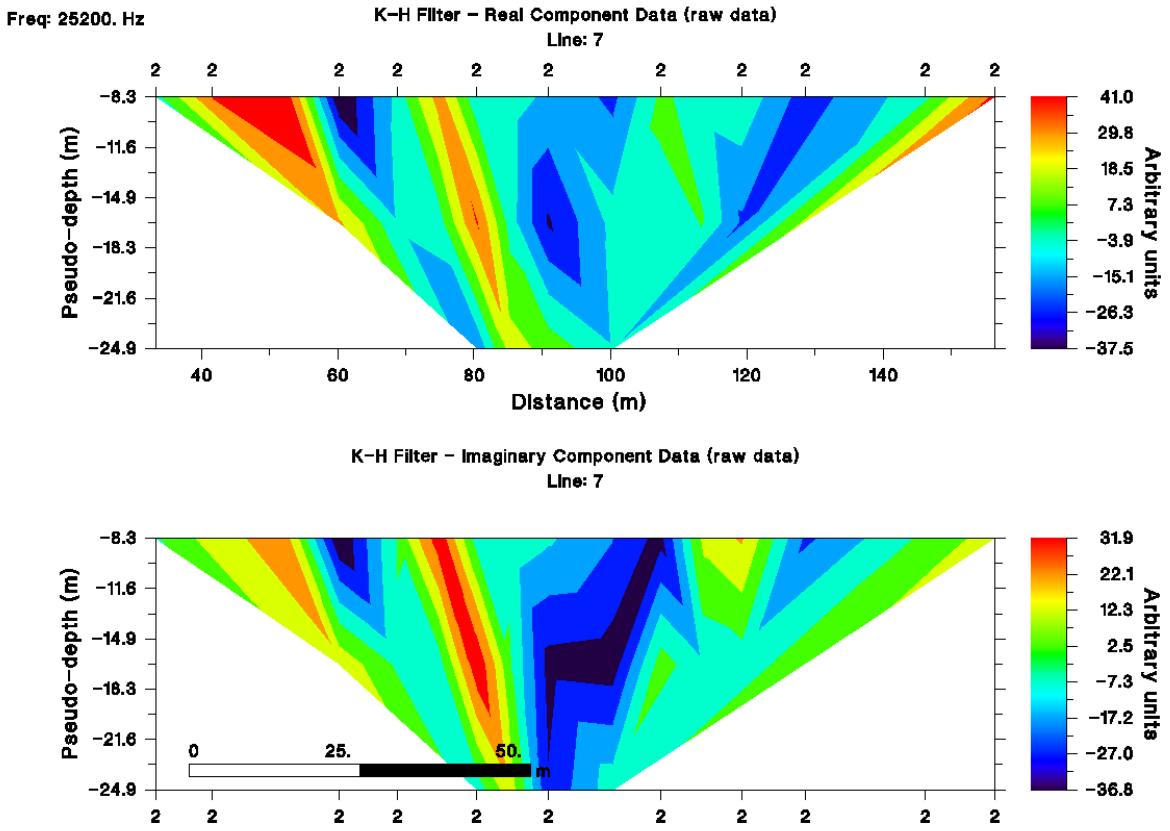

Figure 22: K-H filtered pseudosections modeled from VLF-EM data along profile 7 in Figure 10. Top figure is modeled from the real component and the lower figure is modeled from the imaginary component. Red areas indicate higher conductivity anomalies while blue areas indicate lower conductivity anomalies.

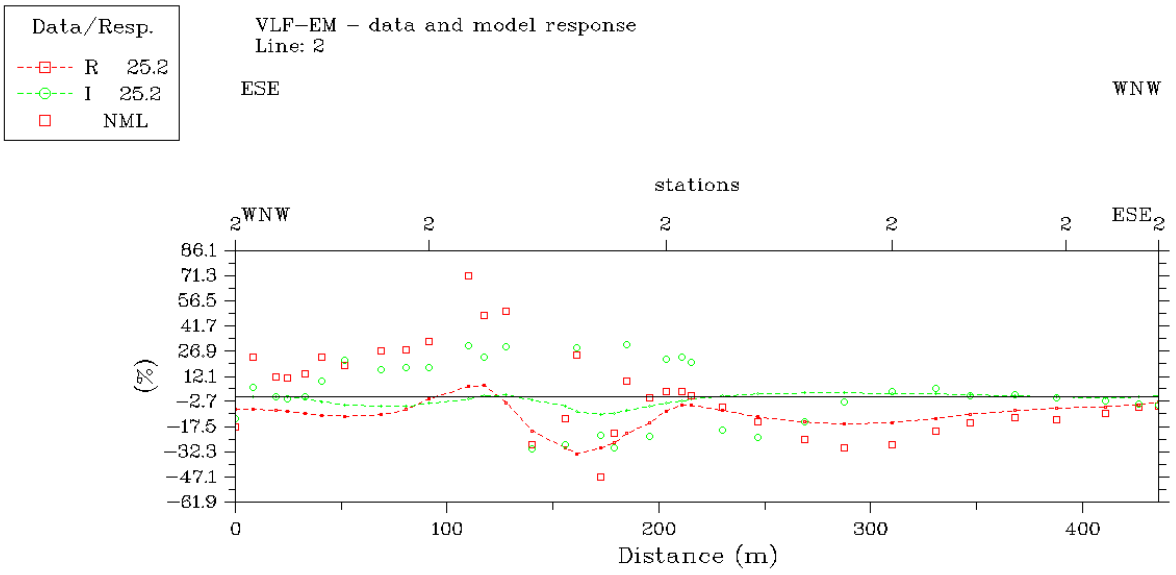

Figure 23: Data (squares) and model (lines) response the below 2D model of the VLF-EM data along profile 2 in Figure 10. Red lines and dots are the real components (IP) while the green dots and lines are imaginary components (OP). This response is from the model produced in figure 23. Rmse = 2.1.

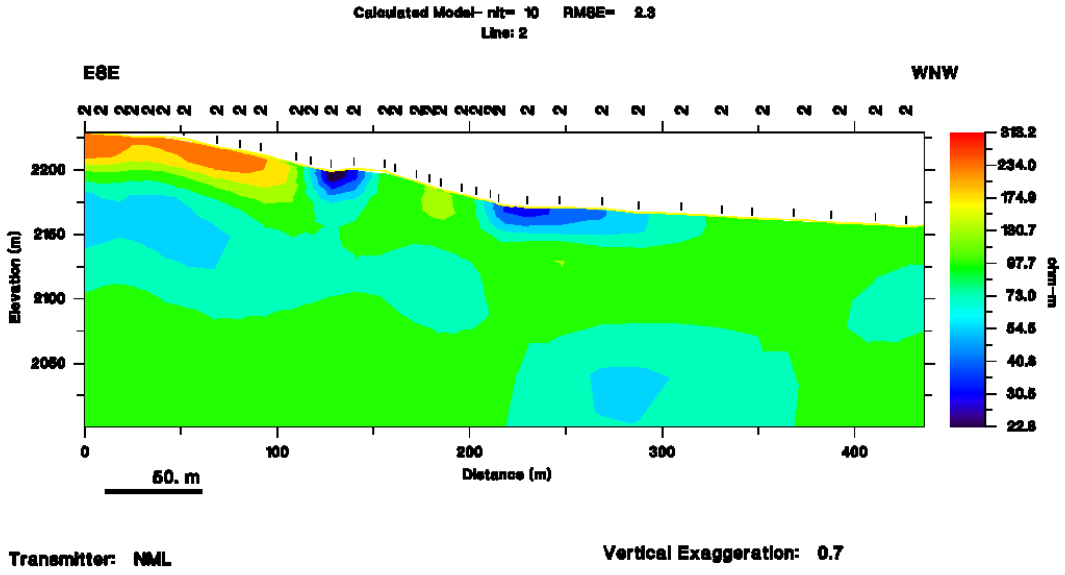

Figure 24: 2D inversion model of VLF-EM data along profile 2 in Figure 10. The starting model was a homogeneous 100 ohm-m earth. Do for all models

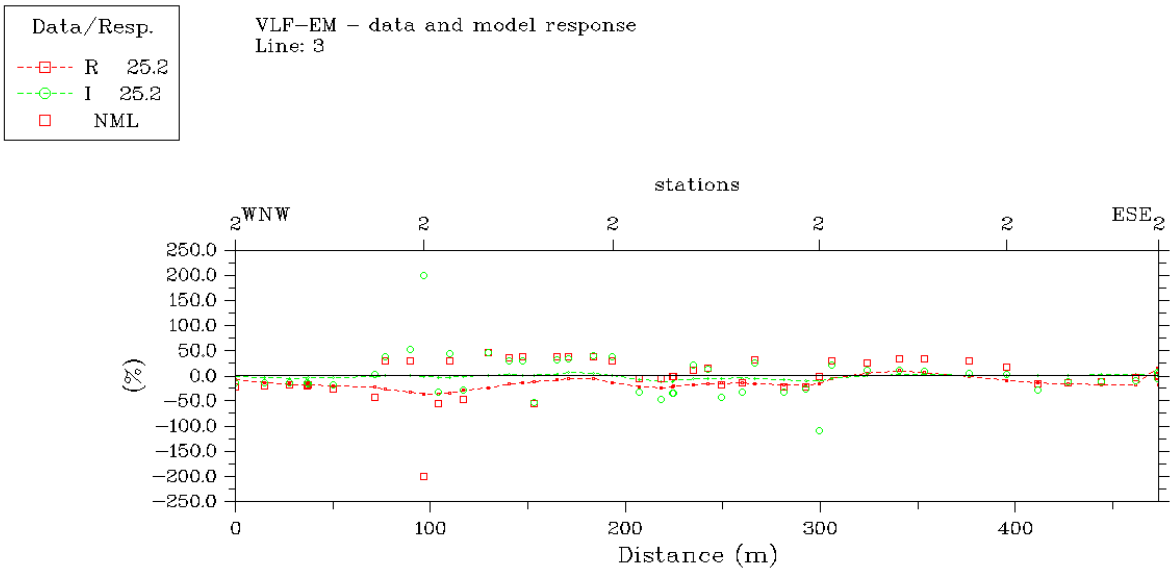

Figure 25: Data and model response to inversion of VLF-EM data along profile 3 in Figure 10. Red lines and dots are the real components while the green dots and lines are imaginary components. This response is from the model produced in figure 25. Rmse = 3.9.

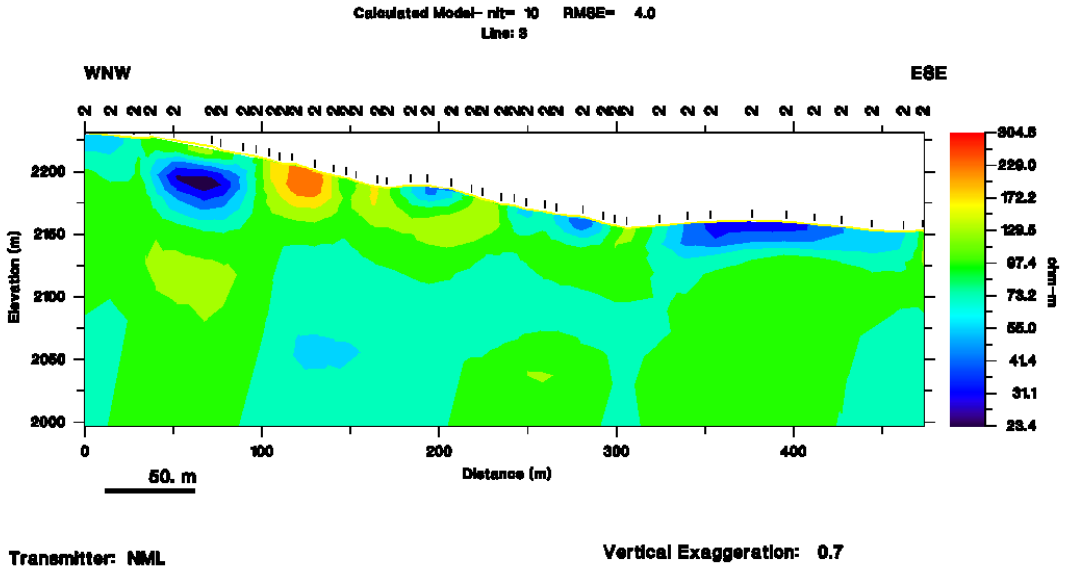

Figure 26: 2D inversion model of VLF-EM data along profile 3 in Figure 10. The starting model was a homogeneous 100 ohm-m earth.

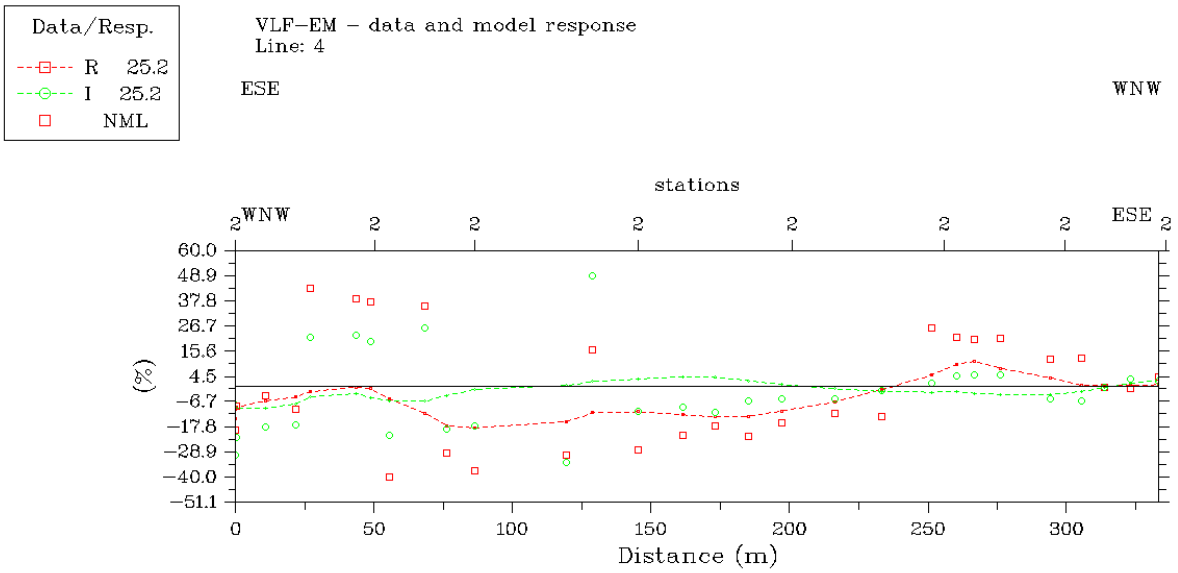

Figure 27: Data and model response to inversion of VLF-EM data along profile 4 in Figure 10. Red lines and dots are the real components while the green dots and lines are imaginary components. This response is from the model produced in figure 27. Rmse = 1.7.

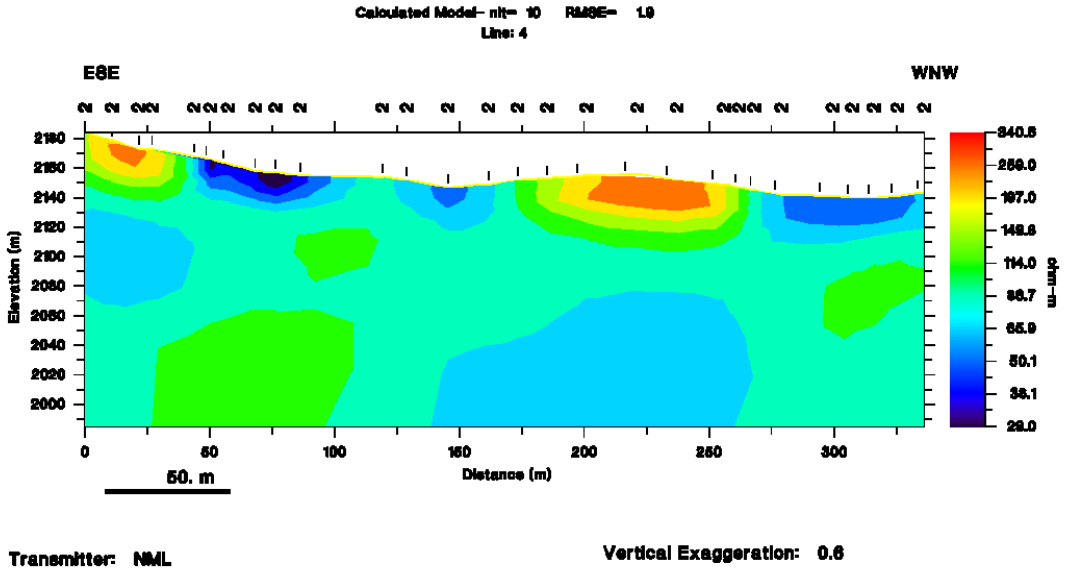

Figure 28: 2D inversion model of VLF-EM data along profile 4 in Figure 10. The starting model was a homogeneous 100 ohm-m earth.

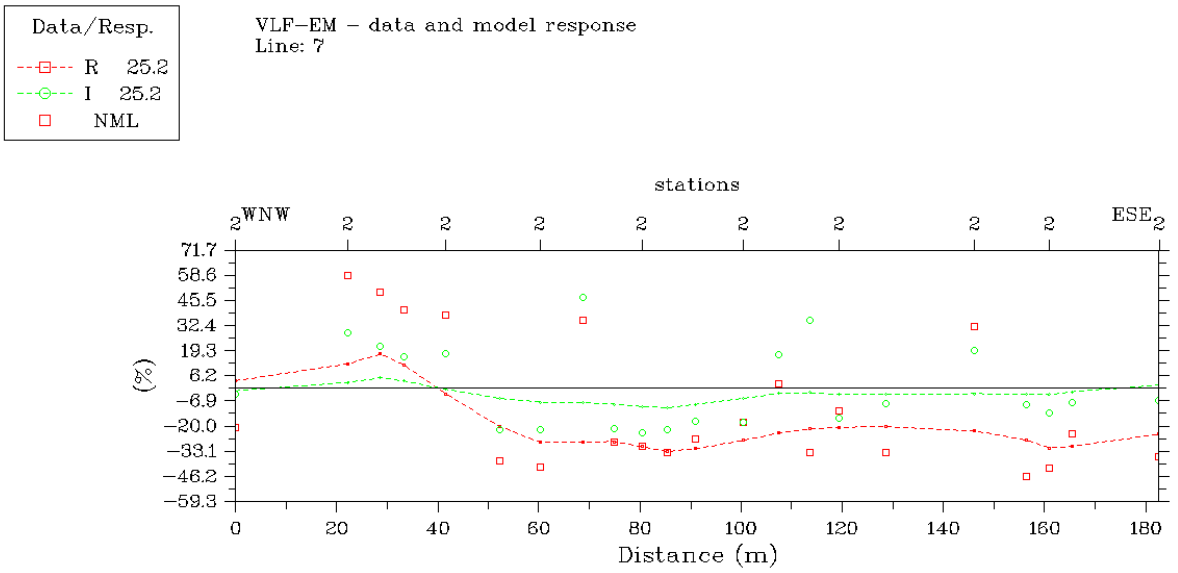

Figure 29: Data and model response to inversion of VLF-EM data along profile 7 in Figure 10. Red lines and dots are the real components while the green dots and lines are imaginary components. This response is from the model produced in figure 29. Rmse = 2.2.

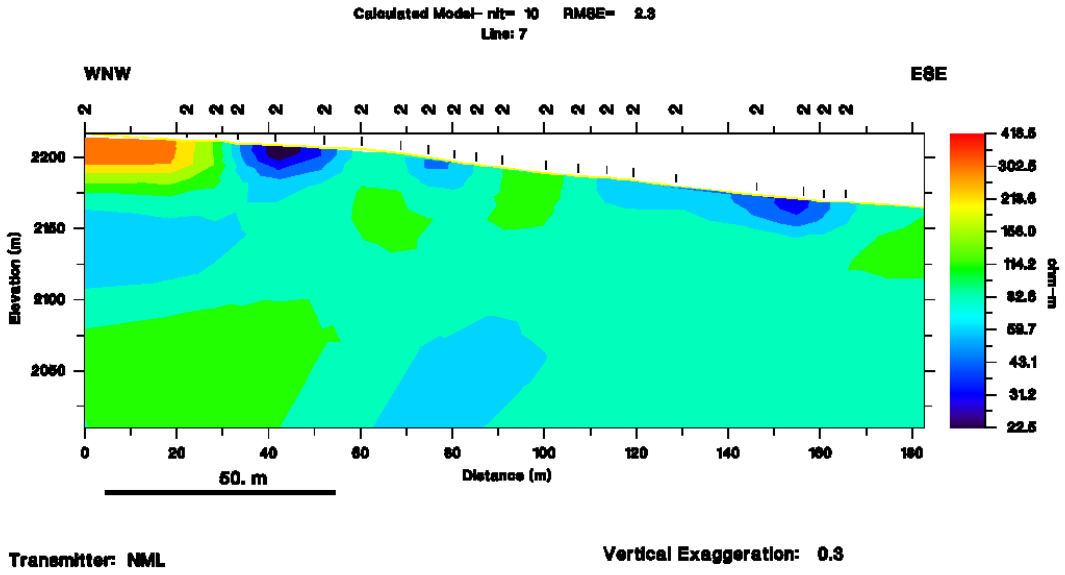

Figure 30: 2D inversion model of VLF-EM data along profile 7 in Figure 10. The starting model was a homogeneous 100 ohm-m earth.

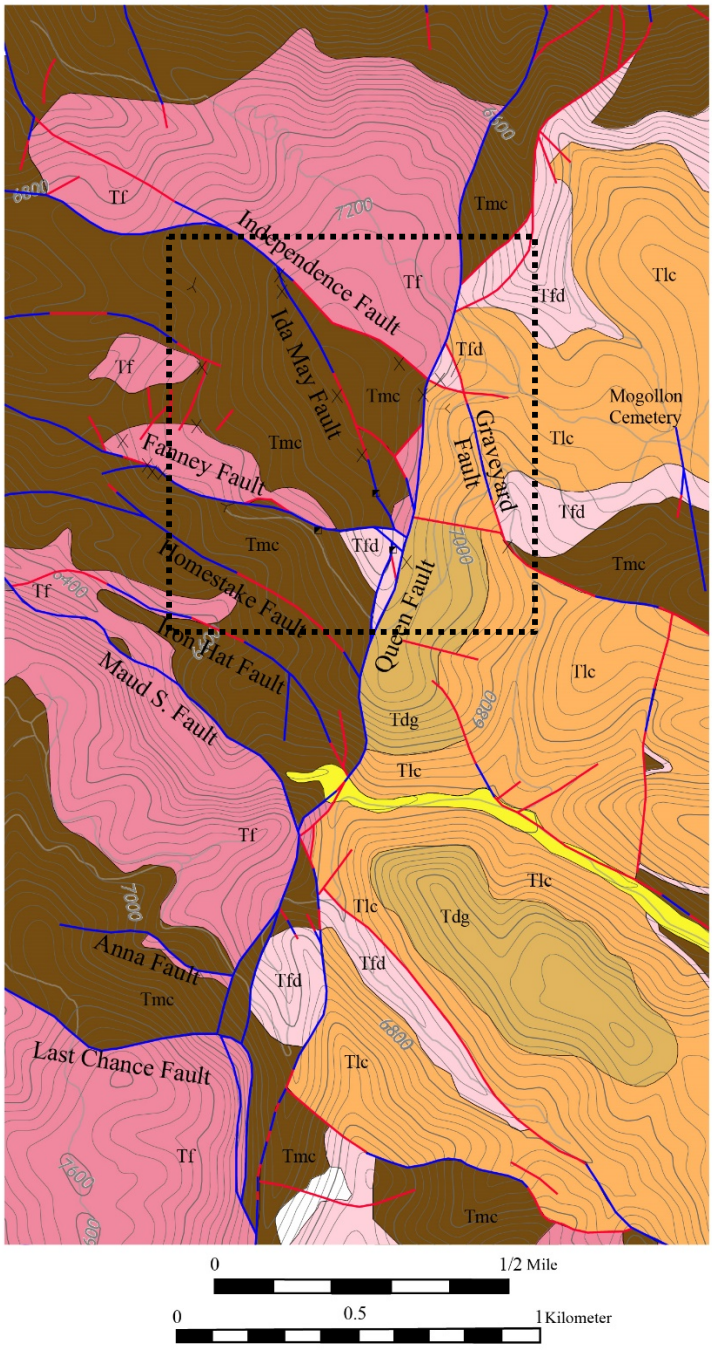

Figure 31: Geologic map with units, faults without mineralization (red), and faults with mineralization (blue). The dashed box denotes the area covered by the magnetic and VLF-EM surveys.

CONCLUSIONS

These manuscripts sought to better understand the geology and structure of the Bearwallow Mountain 7.5-minute quadrangle and the Mogollon Mining District. The first manuscript found that the geology and structures east of the Mogollon Mining District are fundamentally different than those found within the district. The second manuscript found that the Very Low Frequency Electromagnetic system was useful in identifying known and unknown subsurface structures.

We can conclude that veins like those found within the Mogollon Mining District are not found east of the Mogollon 7.5-minute quadrangle. The faults in the Bearwallow Mountain 7.5-minute quadrangle are of a generation that is older than the economic mineralization present in the mining district. This is evidenced by the WNW-ESE nature of most of the faults present, and distinctly different from the dominate N-S faults found in the district. This, therefore contributes to the conclusion that mineralization is associated with the extension of the 19 Ma Mangas Trench. Though the Great Western Fault and the Queen Fault saw little displacement compared to the range-front faults of the Mangas Trench, they still crosscut the older WNW-ESE faults that are older than 24 Ma. Economic mineralization was focused along the Queen fault and does not stray more than a couple kilometers from it. The east is almost barren of veins except for alteration and small mineralization related to late-stage dike emplacement.

The results from the second paper conclude that the Independence fault shows strong conductivity in locations where it does not outcrop on the surface. Furthermore, the Queen fault does not show strong conductors between the Fanney fault and the Graveyard fault. Finally, several smaller faults originally mapped by Ferguson (1927) and ignored by Ratte (1981) and

Hiner (2016) show low resistivity that may also be mineralized. We suggest future the focus of future exploration be along the Independence fault.

REFERENCES

Ferguson, H. G., 1927, Geology and Ore Deposits of the Mogollon Mining District, New Mexico: USGS Bulletin 787.

Ratte, J. C., 1981, Geologic map of the Mogollon quadrangle, Catron County, New Mexico, 1557.

Hiner, J. E., 2016, 43-101 Technical Report on the Mogollon Project, Catron County, New Mexico, USA One World Investments Inc.

APPENDIX

Detailed Unit Descriptions

The following section is a detailed appendix of geologic units found in the Bearwallow Mountain quadrangle. The appendix is arranged from oldest to youngest, and contains mineral descriptions, locations of known outcrops, and maximum exposed thicknesses observed either in the quadrangle or in adjacent quadrangles.

Tas Apache Springs Tuff (Oligocene) – Rhyolite ash flow tuff (ignimbrite). Intra-caldera fill of the Bursum caldera with interbedded volcanoclastic sandstones and volcanic breccia. Generally, the unit is colored reddish-grey to tanish-white, densely welded in some places. Ash-flows are massively bedded and crystal-rich with as much as 50% phenocrysts of quartz,feldspars (sanidine), biotite, rare sphene. Eutaxitic matrix of devitrified pumice and glass shards where not pervasively altered. Volcanoclastic sandstones and conglomerates are interbedded (~10cm – 30cm). Clasts are comprised of rounded tuffaceous material. Minor lithics present. Unit only exposed in the southern third of the quadrangle. Ash-flow tuff is found north of Sandy Point, while the volcanoclastic member is found along Bearwallow Fire Road and near Little Deep Creek. Maximum exposed thickness is ~1,200 feet. Sanidine 40Ar/39Ar age of the Apache Spring tuff reported by McIntosh et al. (1992) is 27.98 ±0.09 Ma.

Tmc Mineral Creek Andesite (Oligocene) – Dark redish-brown lava interlayered with Fanney Rhyolite. Ranges from aphanitic to porphyritic aphanitic. Porphyritic lavas are crystal-rich with phenocrysts of plagioclase and small pyroxene phenocrysts. Type location lavas at the Last Chance Mine in the Mogollon quadrangle yield K-Ar ages of 25.0±0.5 Ma (Strangway et al., 1976). The maximum observed thickness of **Tmc** is ~1,200 feet, observed in Goat Canyon in

the Holt Mountain quadrangle (Ratte, et al., 2006). The unit is very similar to Last Chance Andesite and is difficult to distinguish in the field. The only way to distinguish Tmc and Last Chance Andesite is where the Deadwood Member of the Fanney Rhyolite is present between the units. **Tmc** is only seen on the western edge of the quadrangle in the valley of Mineral Creek. It is stratigraphically below Fanney Rhyolite and the Deadwood Member of the Fanney Rhyolite.

Tf Fanney Rhyolite (Oligocene) – Redish-grey to pinkish-grey rhyolite lava and intrusive domes sourced from ring-fracture domes that developed after the collapse of the Bursum caldera. Aphanitic flows with <1% rounded quartz, plagioclase and rare potassium feldspar and biotite phenocrysts. Potassium feldspar is seen in the groundmass. Porphyritic facies are common with more plagioclase, quartz, and biotite in a sperulitic matix. Pervasively altered near faults. Deposited concurrently with **Tmc**, but is locally above. Deposited prior to **Tfd**. Apparent maximum thickness is 2,300 feet in the south-central portion of the quadrangle.

Tfd Deadwood Gulch Member of Fanney Rhyolite (Oligocene) – Red to pink rhyolite pyroclastic flow and fall deposits overlying Fanney Rhyolite flows, occasionally separated by Tmc lavas. Fall deposits are overlain by Last Chance Andesite. Pyroclastic facies consist of predominantly pumiceous tuff breccia, and partially welded ash-flow tuff. Pumice, lapilli and lithics of flow banded rhyolite are abundant in most locations, while some locations have very little of either. Rarely, lithics consist of unidentifiable metamorphosed sedimentary and pyroclastic volcanic rocks. Pumice is football shaped and occasionally small linear stringers. Ash flows are crystal-rich with phenocrysts of clear quartz, albite, and copper-colored biotite. Reworked facies consist of pyroclastic material, volcanic sandstone and conglomerate as much

as 1 m thick at base of member. Pervasively altered near faults. Stratigraphically above Fanney Rhyolite, and locally below Bearwallow Mountain Andesite or Last Chance Andesite. Apparent maximum thickness about 2,000 feet and thins to the west towards the Mogollon quadrangle.

Twl Willow Creek Latite (Oligocene)– Light grey to pink porphyritic rhyolitic lavas and ash flows. Ash flows contain abundant pumice and large sanidine phenocrysts with rims of plagioclase. Some black biotite and little to no quartz. Unit was originally described by Ratte and Gaskill (1975) and interpreted to be a dome complex related to the Bursum caldera. **Twl** is found on the eastern edge of the quadrangle, south of Bearwallow Mountain, and north of NM-159. It appears to be stratigraphically above **Tf**, and down dropped next to **Tas**. More mafic facies of **Twl** are found in the adjacent Negrito Mountain quadrangle (written commun. Matt Zimmerer, 2019).

Tlc Last Chance Andesite (Oligocene) – Thick sequence dark grey to redish-brown aphanitic andesite lava flows, locally above Deadwood Gulch member of the Fanney Rhyolite. Unconformabley below Dog Gulch Conglomerate and Bearwallow Mountain Andesite. Last Chance lavas are suggested to be part of the moat-fill sequence around the resurgent dome of the Bursum caldera. Contain rare phenocrysts of plagioclase and pyroxene. Indistinguishable from Mineral Creek Andesite unless Deadwood member of Fanney Rhyolite is present. Lenses of sandstone approximately 3 meters thick are present along Copper Creek Road. Ratte (1981) reported the K-Ar age between 25.0 ± 0.6 Ma along Houston Canyon and 23.2 ± 0.6 Ma west of Bearup Springs in the Mogollon quadrangle. Flows occurred concurrently with Bearwallow Mountain Andesite, though **Tba** appears to have erupted in the eastern portion of the quadrangle

while **Tlc** erupted in the west. Vent may be located at Cooney Peak or Spring Mountain due to the thicknesses observed.

Tba Bearwallow Mountain Andesite (Oligocene) – Dark grey vesicular to amygdaliodial aphanitic basaltic andesite and andesite lavas. Some sequences contain small olivine (iddingsite) and hypershene,but the lavas are overall crystal-poor. A vent is suggested at Bearwallow Mountain for this unit as it thins in all directions from the peak. Individual flows are thin ranging from <1 m to 10 m. Willow Creek (southeastern corner of the quadrangle) exposes ~400 feet of Bearwallow Mountain Andesite, which suggests that the entire quadrangle was once covered by the unit. Small windows along Copper Creek expose lower units (Fanney Rhyolite and Deadwood Member) signifying a paleo-topographic high. Apparent maximum thickness at least 1,000 feet in the northern section of the quadrangle.

Tdg Dog Gulch Conglomerate (Miocene?) – Post-volcanic sandstones and conglomerates. Exposures in the western quadrangle are comprised of buff sandstones with thin interbedded conglomerates. In some locations, the unit is crosscut by andesite dikes. **Tdg** filled in existing basins in the north-western area of the quadrangle, on lapping existing scarps of **Tas** and **Tlc**. **Tdg** is younger than all units except for Quaternary alluvium found in present-day valleys. Miocene age based on 15.2±0.2 Ma date based on Basalt that overlies the Dog Gulch east of the Bearwallow Mountain quadrangle. Thickness is 0-200 m near west-central border with the Mogollon quadrangle.

Qa Alluvium (Holocene) – Undifferentiated and unlithified sands and conglomerates deposited form modern streams. Generally only a few feet thick, but up to 12 feet (Deep Creek Canyon).

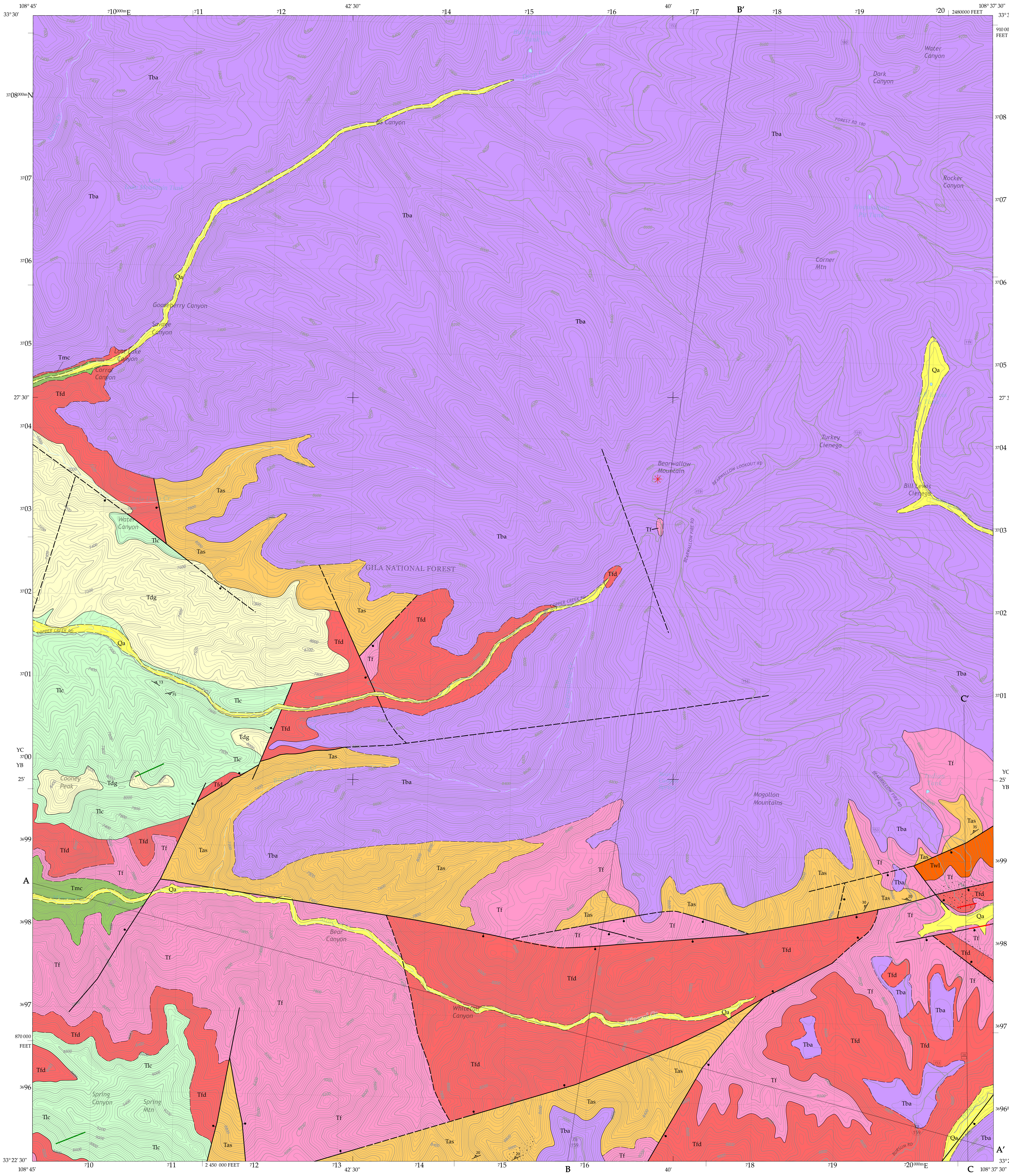

Correlation of Map Units

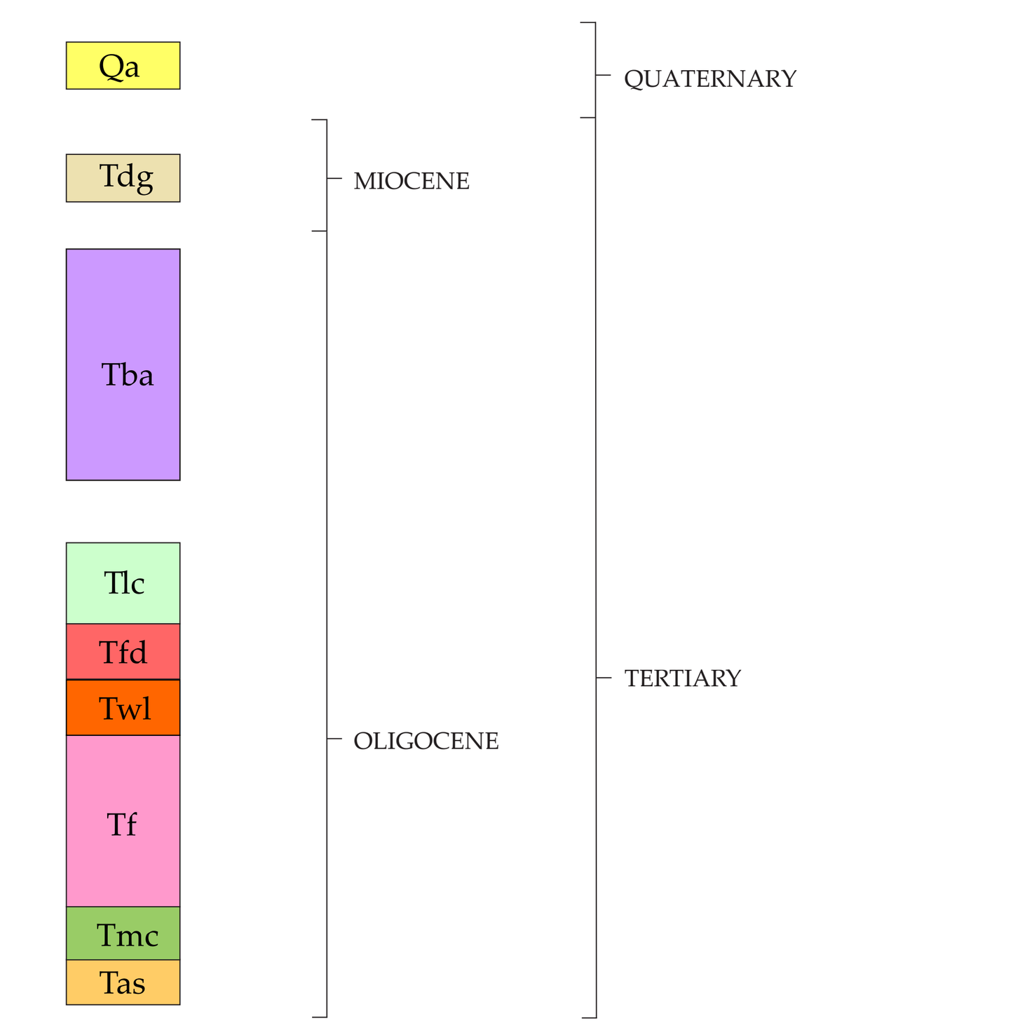

Contact

Inferred Contact

Normal Fault; Ball on downthrown side

Generic Verticle Foliation

Generic Dipping Foliation

Inferred Normal Fault

Silicic and Argillic alteration

Andesite Dike

Rhyolite Dike

Horizontal Bedding

Volcanic Vent

Description of Map Units

Qa — **Alluvium (Holocene)** – Undifferentiated and unlithified sands and conglomerates deposited form modern streams. Generally only a few feet thick, but up to 12 feet (Deep Creek Canyon).

Tdg — **Dog Gulch Conglomerate (Miocene?)** – Post-volcanic sandstones and conglomerates. Exposures in the western quadrangle are comprised of buff sandstones with thin interbedded conglomerates. In some locations, the unit is crosscut by andesite dikes. Tdg filled in existing basins in the north-western area of the quadrangle, on lapping existing scarps of Tas and Tlc. Tdg is younger than all units except for Quaternary alluvium found in present-day valleys.

Tba — **Bearwallow Mountain Andesite (Oligocene)** – Dark grey vesicular aphanitic basaltic andesite. Some sequences contain small olivine, but the flows are overall crystal poor. Bearwallow Mountain is a suggested vent location for this unit as it thins in all directions from the peak. Willow Creek (southeastern corner of the quadrangle) exposes ~400 feet of Bearwallow Mountain Andesite, which suggests that the entire quadrangle was once covered by the unit. Small windows along Copper Creek expose lower units (Fanney Rhyolite and Deadwood Member) signifying a paleo-topographic high. Apparent maximum thickness at least 1,000 feet in the northern section of the quadrangle.

Andesite Dike (Oligocene) – Fine grained andesitic dikes that intrude Tdg and Tlc. Thickness less than 1 meter.

Tlc — **Last Chance Andesite (Oligocene)** – Dark grey to redish-brown aphanitic lava flows locally above Deadwood Gulch member of the Fanney Rhyolite. Unconformabley below Dog Gulch Conglomerate and Bearwallow Mountain Andesite. Contain rare phenocrysts of plagioclase and pyroxene. Indistinguishable from Mineral Creek Andesite unless Deadwood member of Fanney Rhyolite is present. Lenses of sandstone approximately 3 meters thick are present along Copper Creek Road. Ratte (1981) reported the K-Ar age between 25.0 ± 0.6 million years and 23.2 ± 0.6 million years. Flows occurred concurrently with Bearwallow Mountain Andesite, though Tba appears to have erupted in the eastern portion of the quadrangle while Tlc erupted in the west. Vent may be located at Cooney Peak or Spring Mountain due to the thicknesses observed.

Twl — **Willow Creek Latite (Oligocene)** – Light grey to pink porphyritic lava. Abundant pumice and large sanidine phenocrysts with rims of plagioclase. Some black biotite and little to no quartz. Unit was originally described by Ratte and Gaskill (1975) and interpreted to be a dome complex related to the Bursum caldera. Twl is found on the eastern edge of the quadrangle, south of Bearwallow Mountain, and north of NM-159. It appears to be stratigraphically above Tf, and down dropped next to Tas. More mafic facies of Twl are found in the adjacent Negrito Mountain quadrangle (written comm. Matt Zimmerer, 2019).

Rhyolite Dike (Oligocene) – Silicified fine grained dikes ~1-2 meters wide. Rare unaltered biotite. Associated with Tfd in SE corner of quadrangle.

Tfd — **Deadwood Gulch Member of Fanney Rhyolite (Oligocene)** – Red to pink pyroclastic flow and fall deposit overlying Fanney Rhyolite flows. Partially welded pumice and licthics are abundant in most locations, while some locations have very little of either. Lithics consist of unidentifiable metamorphosed sedimentary and volcanic rocks. Pumice is football shaped and occasionally small linear stringers. Clear quartz, albite, and copper-colored biotite phenocrysts. Pervasively altered near faults. Stratigraphically above Fanney Rhyolite, and locally below Bearwallow Mountain Andesite or Last Chance Andesite. Apparent maximum thickness about 2,000 feet.

Tmc — **Mineral Creek Andesite (Oligocene)** – Dark redish-brown lava flows interlayered with Fanney Rhyolite. Unit is very similar to Last Chance Andesite and is difficult to distinguish in the field. Tmc is only seen on the westen edge of the quadrangle in the valley of Mineral Creek. It is stratigraphically below Tf and Tfd.

Tf — **Fanney Rhyolite (Oligocene)** – Redish-grey to pinkish-grey rhyolite flows sourced from ring-fracture domes that developed after the collapse of the Bursum caldera. Aphanitic flows with rounded quartz phenocrysts and rare potassium feldspar phenocrysts. Potassium feldspar is seen in the groundmass. Porphyritic facies are common with more plagioclase, quartz, and biotite. Pervasively altered near faults. Deposited concurrently with Tmc, but is locally above. Deposited prior to Tfd. Apparent maximum thickness is 2,300 feet in the south-central portion of the quadrangle.

Tas — **Apache Springs Tuff (Oligocene)** – Intra-caldera fill of the Bursum caldera consisting of rhyolite ash-flow tuffs, and volcanoclastic sandstones and conglomerates. Generally colored reddish-grey to tanish-white. Ash-flows are massively bedded with phenoctysts of small quartz and in some cases large feldspars (sanidine), black biotite, rare sphene; pumice and glass make up the matrix. Volcanoclastic sandstones and conglomerates are interbedded (~10cm – 30cm). Clasts are comprised of rounded tuffaceous material. Minor lithics present. Unit only exposed in the southern third of the quadrangle. Ash-flow tuff is found north of Sandy Point, while the volcanoclastic member is found along Bearwallow Fire Road and near Little Deep Creek. Maximum exposed thickness is ~1,200 feet.

Geochronology

This section will discuss the geochronology of units found within the Bearwallow Mountain quadrangle. All of the geochronology studies listed below were done outside of the quadrangle, however they give good constraints on ages. $^{40}Ar/^{39}Ar$ geochronology data from Mcintosh et al. (1992) place the Apache Springs Tuff (Tas) (27.98 ± 0.09 Ma), and the Bloodgood Canyon Tuff (28.05 ± 0.04 Ma) are statistically imperceptible are within analytical error. Earlier data by Elston et al. (1973) report a biotite K-Ar ages of Tas to be 27.3 ± 0.8 Ma. The Fanney Rhyolite (Tf) has a reported K-Ar age of 26.0 Ma and 24.4 Ma from Bikerman et al. (1992). Deadwood Gulch member of the Fanney Rhyolite (Tfd) is undated, but in the Mogollon quadrangle, it is stratigraphically between Mineral Creek Andesite and Last Chance Andesite. Mineral Creek Andesite (Tmc) was dated by Strangway et al. (1976) using whole-rock K-Ar and found an age of 25.0 ± 0.5 Ma. Last Chance Andesite (Tlc) was also dated using whole-rock K-Ar methods that produced ages of 25.0 ± 0.6 Ma and 23.2 ± 0.6 Ma. Bearwallow Mountain Andesite (Tba) has an $^{40}Ar/^{39}Ar$ age of 24 Ma (McIntosh et al., 1992). The Deadwood member of the Fanney Rhyolite and Willow Creek Latite are undated.

Unit	Method	Age	Error	# Analyses	Source
Tas	$^{40}Ar/^{39}Ar$	27.98	0.09	3	McIntosh et al., 1992
Tbc	$^{40}Ar/^{39}Ar$	28.05	0.04	8	McIntosh et al., 1992
Tf	K - Ar	26 - 24.4	?	2	Bikerman et al., 1992
Tmc	Wholerock K-Ar	25	0.5	?	Strangway et al., 1976
Tlc	Wholerock K-Ar	25 - 23.2	0.6	1	Ratte, 1981
Tba	Paleomagnetic	< 24	?	1	McIntosh et al., 1992

References

Bikerman, M., Bell, K., and Card, J. W., 1992, Strontium and neodymium isotopic study of the Western Mogollon-Datil Volcanic region, New Mexico, USA: Contributions to Mineralogy and Petrology v. 109, p. 459-470.

Elston, W.E., Damon, P.E., Coney, P.J., Rhodes, R.C., Smith, E.I., Bikerman, M., 1973, Tertiary Volcanic Rocks, Mogollon-Datil Province, New Mexico, and Surrounding Region: K-Ar Dates, Patterns of Eruption, and Periods of Mineralization: Geological Society of America Bulletin, v. 84, p. 2259-2274.

McIntosh, W. C., Chapin, C. E., Ratte, J. C., and Sutter, J. F., 1992, Time-stratigraphic framework for the Eocene-Oligocene Mogollon-Datil Volcanic Field, Southwest New Mexico: Geological Society of America Bulletin, v. 104, no. 7, p. 851-871.

Ratte, J. C., and Gaskill, D. L., 1975, Reconnaissance geologic map of the Gila Wilderness study area, southwestern New Mexico: U.S. Geological Survey Miscellaneous Geological Inventory Map I-886.

Ratte, J. C., 1981, Geologic map of the Mogollon quadrangle, Catron County, New Mexico, U.S. Geological Survey GQ- 1557, scale 1:24 000, 1 sheet.

Strangway, D.W., Simpson, J., and York, D., 1976, Paleomagnetic studies of volcanic rocks from the Mogollon plateau area of Arizona and New Mexico: New Mexico Geological Society Special Publication 5, p. 119-124.

North American Datum of 1983 (NAD83)
World Geodetic System of 1984 (WGS84). Projection and 1 000-meter grid: Universal Transverse Mercator, Zone 12S
10 000-foot ticks: New Mexico Coordinate System of 1983 (west zone)

SCALE 1:24 000

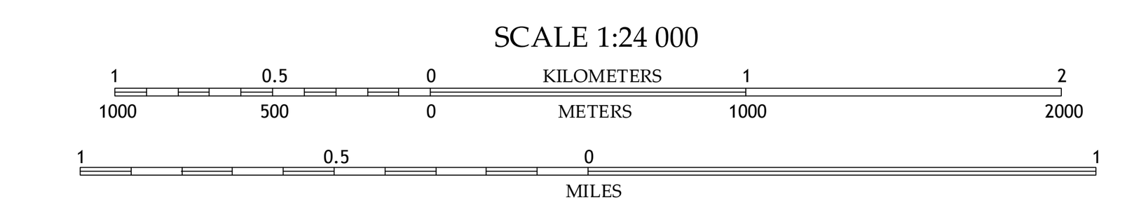

CONTOUR INTERVAL 40 FEET
NORTH AMERICAN VERTICAL DATUM OF 1988

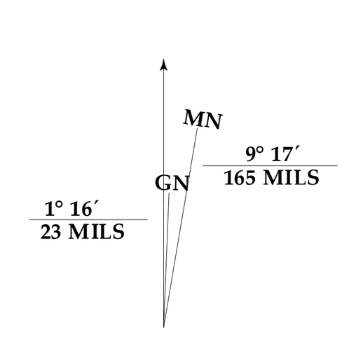

1	2	3
4		5
6	7	8

1 O Block Canyon
2 Sign Camp Mountain
3 Telephone Canyon
4 Mogollon
5 Negrito Mountain
6 Holt Mountain
7 Grouse Mountain
8 Mogollon Baldy Peak

ADJOINING QUADRANGLES

Geologic Map of the Bearwallow Mountain 7.5-Minute Quadrangle, Catron County, New Mexico

December, 2019

Charles F. Hoffman, Gary S. Michelfelder, Loren Bohannon, Megan Peitz

Missouri State University, 901 S National Ave., Springfield, MO 65897

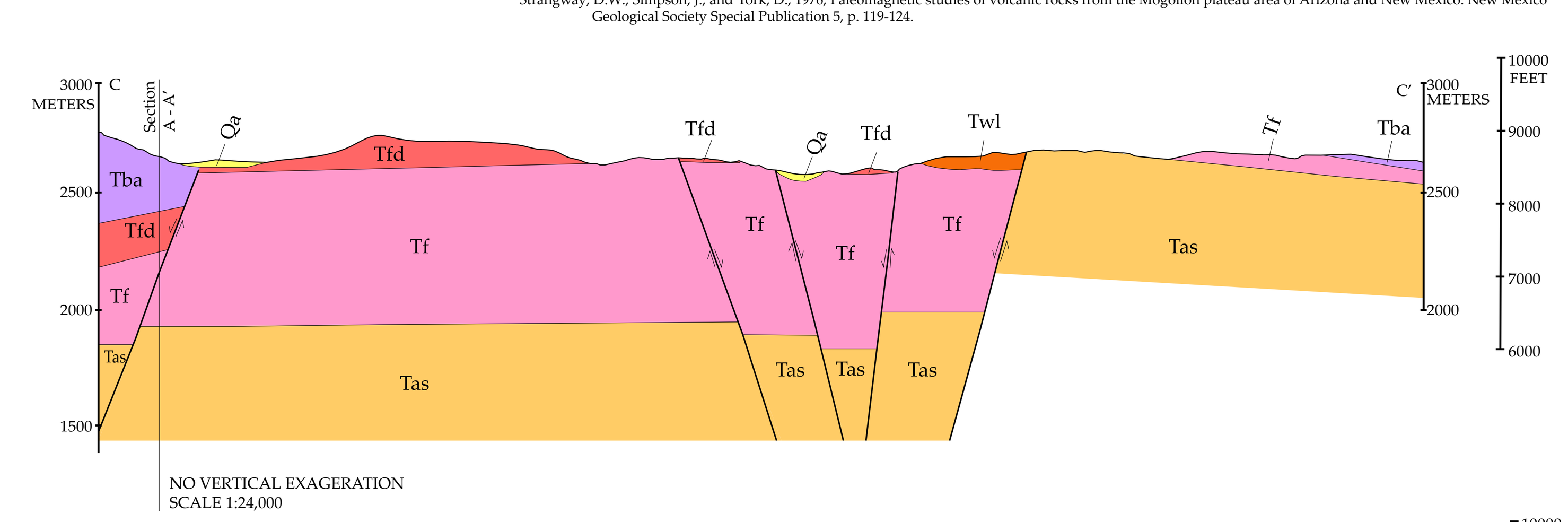

NO VERTICAL EXAGERATION
SCALE 1:24,000

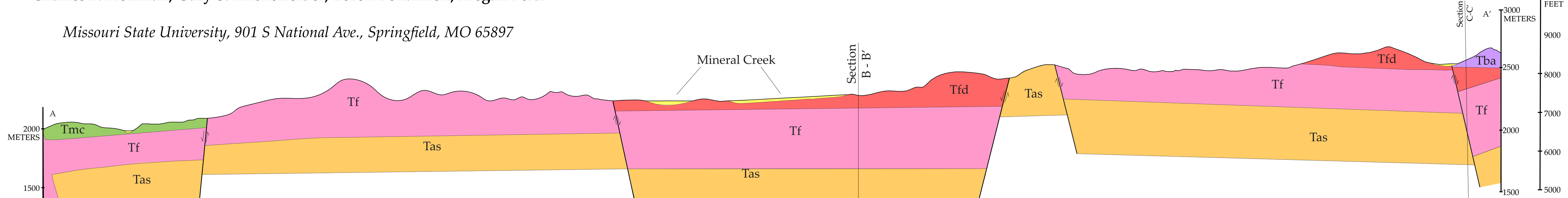

NO VERTICAL EXAGERATION
SCALE 1:24,000

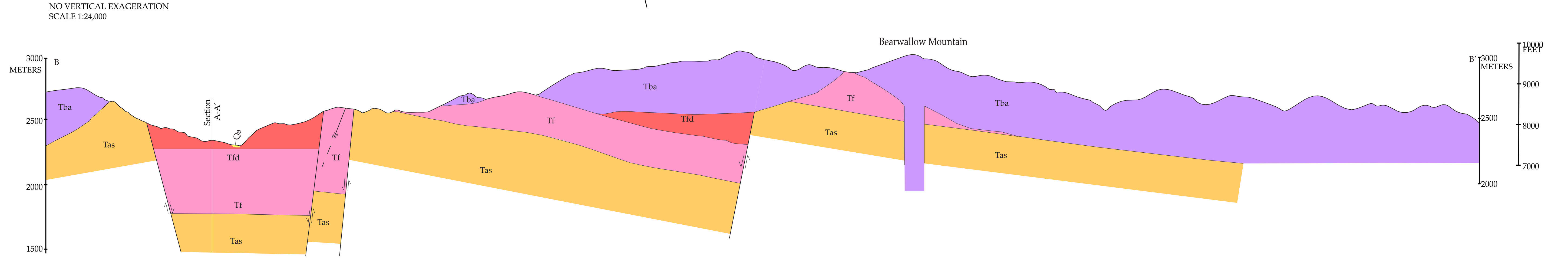

Comments to Map Users

A geologic map displays information on the distribution, nature, orientation, and age relationships of rock and deposits and the occurrence of structural features. Geologic and fault contacts are irregular surfaces that form boundaries between different types or ages of units. Data depicted on this geologic quadrangle map may be based on any of the following: reconnaissance field geologic mapping, compilation of published and unpublished work, and photogeologic interpretation. Locations of contacts are not surveyed, but are plotted by interpretation of the position of a given contact onto a topographic base map; therefore, the accuracy of contact locations depends on the scale of mapping and the interpretation of the geologist(s). Any enlargement of this map could cause misunderstanding in the detail of mapping and may result in erroneous interpretations. Site-specific conditions should be verified by detailed surface mapping or subsurface exploration. Topographic and cultural changes associated with recent development may not be shown.

Cross sections are constructed based upon the interpretations of the author made from geologic mapping, and available geophysical, and subsurface (drillhole) data. Cross-sections should be used as an aid to understanding the general geologic framework of the map area, and not be the sole source of information for use in locating or designing wells, buildings, roads, or other man-made structures.

The map has not been reviewed according to New Mexico Bureau of Geology and Mineral Resources standards. The contents of the report and map should not be considered final and complete until reviewed and published by the New Mexico Bureau of Geology and Mineral Resources. The views and conclusions contained in this document are those of the authors and should not be interpreted as necessarily representing the official policies, either expressed or implied, of the State of New Mexico, or the U.S. Government.